Wear 396–397 (2018) 107–125

Contents lists available at ScienceDirect

Wear

journal homepage: www.elsevier.com/locate/wear

# Validation of a constitutive law for friction-induced vibration under different wear conditions

A. Cabboi, J. Woodhouse*

*Department of Engineering, University of Cambridge, Trumpington Street, Cambridge CB2 1PZ, U.K.*

ARTICLE INFO

*Keywords:*
Dynamic friction
Contact stiffness
Rate-and-state models
Structural vibration
Model validation

ABSTRACT

Recent work (Cabboi et al. [1]) has shown promising agreement between measurements and theoretical modelling of high-frequency dynamic sliding friction. This paper confirms and extends this agreement by presenting results for a wide selection of contacting materials. Additional measurement techniques are also introduced, to give independent confirmation of parameter identification and improve the robustness of the identification process. The results show that virtually every individual measurement can be fitted accurately by the proposed theoretical model, and that in all cases where rapid wear of the contacting materials was not an issue it was possible to achieve a good global fit to sets of tests at different normal loads and sliding speeds. The evidence suggests that this measurement procedure is able to characterise the dynamic behaviour at a frictional interface up to kiloHertz frequencies, and consequently provide the means to discriminate among, and calibrate, proposed dynamic friction models. Identifying a reliable model could significantly improve the prediction accuracy for friction-induced vibration such as vehicle brake squeal.

## 1. Introduction

Friction is an essential ingredient of many engineering systems, as in devices like brakes or clutches where force transmission plays a key role. In others it is an unwanted phenomenon, for example resulting in loss of accuracy in positioning control or the appearance of self-excited vibration such as brake squeal. In either case it is important to be able to predict and control the dynamic friction force, but this has proved to be a very elusive goal: see for example [2,3]. Friction-related phenomena have a reputation for "twitchiness": in an experimental setting it is hard to obtain reliable and repeatable results. This suggests sensitivity to factors that are not well controlled or characterised [4], and it makes careful validation tests of theoretical models challenging.

The literature offers many attempts to decrypt the puzzling physics behind frictional interaction by proposing physics-based or phenomenological friction laws. The first type of constitutive law is typically based on integrating the mechanical principles applied at a microscopic scale (which might mean the molecular level or the asperity level) over the whole contact surface: see for example [5–11]. Such models require information concerning the geometry, such as the roughness distribution and the contact configuration (usually parameterised by the indentation depth), and the material properties including a characterisation of deliberate or accidental additional material near the sliding interface (be it an oxide layer, lubricant film or "leaves on the line"). On the other hand, phenomenological models are based on fitting to empirical observations: examples range from the familiar Amontons-Coulomb law or simple viscous friction, to more complicated effects such as time-evolving static friction and frictional memory. Different combinations of observed phenomena have led to more complex models such as the Stribeck-type model [12,13], rate-and-state models [14–18], LuGre model [19,20], or enhanced versions of the Maxwell-slip model [21,22].

When it comes to the quantitative prediction of friction-induced vibration, the focus of the present work, the application of existing friction models does not have a good track record. It has been argued elsewhere that the major reason lies in the absence of appropriate, validated constitutive laws for dynamic friction [23]: the requirements become increasingly stringent as the question of interest changes from stability thresholds, to limit-cycle waveforms, to detailed transient responses. This remark applies to a wide range of different systems, including earthquakes [24–26], violin strings ([27,28]), vehicle brakes [29,30] and friction dampers in gas turbine fans [31,32].

In practice, empirical information about friction is most commonly obtained from standardised tribological tests performed at macro-scale, based on imposed steady sliding or reciprocating sliding [4]. Some variables may be taken into account: the contact configuration, the material combination, the sliding speed, the normal force and the testing environment (e.g. dry friction, lubricated friction, temperature,

* Corresponding author.
*E-mail address:* jw12@cam.ac.uk (J. Woodhouse).

http://dx.doi.org/10.1016/j.wear.2017.08.010
Received 20 April 2017; Received in revised form 28 August 2017; Accepted 28 August 2017
Available online 31 August 2017

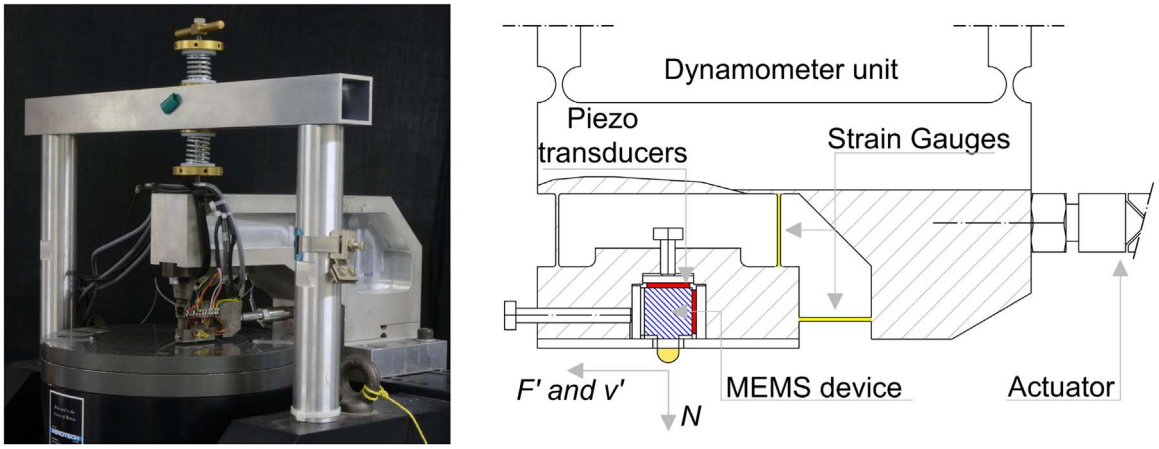


**Fig. 1.** General view of the pin-on-disc rig and detailed view of the installed sensor package in the dynamometer unit.

humidity). The deduced friction "laws" are then often naively applied in attempts to predict the dynamic friction behaviour at relatively high frequencies, where friction-induced vibration commonly occurs [2,33–35].

It has been demonstrated in previous work that this approach is fundamentally flawed [36,30,23,1], even when applied to the simplest question about friction-induced vibration: to predict the threshold of instability when steady sliding gives way to exponentially-growing vibration of sufficiently small amplitude to be governed by linear theory. Under those circumstances, it is easy to determine the correct way to characterise the relevant aspects of frictional behaviour. As will be summarised in the next section, the requirement is for a kind of frequency response function for sliding friction. A test rig to measure this quantity has been described [1], and sample results have been shown for a restricted selection of contacting materials. It was found empirically that this frictional frequency response was remarkably free of the traditional "twitchiness" of friction measurements: reliable and repeatable results were obtained even under circumstances when the *steady* friction characteristics did indeed exhibit such variability. This shows two things: that the new quantity is in some ways easier to pin down than traditional measures of friction, and that it behaves in a manner that is significantly decoupled from the steady-sliding behaviour.

Furthermore, it has been shown that the frictional frequency response offers a sensitive new tool for discriminating between candidate theoretical models. Some existing models from the literature could be definitively ruled out, at least for the particular material combinations used in these tests, nylon or polycarbonate against glass [37]. A class of models was then discussed, which combined the "rate and state" methodology with the influence of contact stiffness [1]. It was shown that models of this type can account very well for the observed behaviour (for the particular materials tested): not only was it possible to match any individual measurement to the model, but some key aspects of parameter dependence on the mean sliding speed and normal force were well captured.

In the light of these promising results, the next stages of research are easy to map out. It is first important to know whether a similar level of agreement can be achieved with a wider range of materials. In the process, it is useful to refine the measurement and parameter estimation processes to streamline the stages and also to provide internal consistency checks between alternative approaches to measuring the same quantity. These are the tasks of the present paper. The next logical step might be to incorporate models of this kind into commercial computer software, such as Finite Element codes, typically used by industrial designers when attempting to develop such things as non-squealing brake systems.

## 2. Background summary

### 2.1. The frictional frequency response

Consider a sliding friction interaction between two mechanical systems, making contact at a single point. Suppose that the steady sliding speed $v_0$ is modulated by a small oscillatory disturbance $v'$ at angular frequency $\omega$, so that:

$$v \approx v_0 - v' e^{i\omega t}. \tag{1}$$

If linear theory is applicable, the evoked frictional force must take the form:

$$F \approx F_0 + F' e^{i\omega t} \tag{2}$$

where $F_0$ and $F'$ are the steady-state and perturbed amplitudes of the friction force, respectively. The negative sign in Eq. (1) is chosen for consistency with earlier work ([36]). The ratio of the two perturbation amplitudes encapsulates the required information about dynamic friction, in the form of a frequency response function $\beta(\omega)$:

$$\beta(\omega) = \frac{F'(\omega)}{v'(\omega)}. \tag{3}$$

It is in general a complex number, specifying the amplitude and phase of the force perturbation relative to the speed perturbation, both of which may possibly vary with frequency. It is the natural quantity to enter any linearised calculation of the threshold of friction-induced vibration. A linear computational framework has indeed been extensively used for brake squeal applications ([33,13,35]) and earthquake processes ([24–26]), requiring a linearised constitutive law of dynamic friction of this general type.

### 2.2. Measurement rig

A test rig has been developed to measure $\beta(\omega)$ ([36]). It is based on a pin-on-disc design, in which a small hemispherical pin sample of one material is pressed against a disc of a second material fixed to a controllable rotary stage (see Fig. 1). The pin assembly incorporates an actuator to allow a small dynamical modulation of the effective sliding speed as envisaged in Eq. (1), and also a package of sensors to allow the dynamic force and motion to be monitored. Standard techniques for measuring the frequency response function of a linear system can then be applied (see for example [38]): band-limited pseudo-random noise is used for the input, and averaging is used to give a stable estimate of $\beta(\omega)$ together with the associated coherence function (as a check on linearity). A full description of the experimental rig, the sensor calibration procedure and the measurement process was given in [1]. It should be emphasised that this measurement relies on response to

forced vibration: although the ultimate goal of the research is the reliable prediction of self-excited frictional vibration, such spontaneous vibration ("squeal") must be avoided during this testing.

So far, only a few measurements of $\beta(\omega)$ have been published ([36,1]). Two different material combinations have been systematically explored: a nylon pin against a glass disc and a polycarbonate pin against a glass disc. These were tested with all combinations of a set of sliding speeds and a set of mean normal forces. A puzzling feature, which still needs to be clarified, is the excellent repeatability of the measured frictional frequency response. The usual testing procedure consists in choosing a normal force and a sliding-speed range. A series of tests is then conducted with the different sliding speeds, holding the normal force fixed. Speeds are tested first in an increasing and subsequently a decreasing order. As a result, each particular case of $\beta(\omega)$ and the associated mean friction coefficient $\mu_{ss}$ is estimated twice at different stages in the test sequence. For both material combinations, the $\beta(\omega)$ measurements proved to be much more repeatable than $\mu_{ss}$. In fact, the latter was often found to exhibit quite different values for the same sliding speed before and after a sequence of tests, sometimes changing by a factor of two or more.

### 2.3. Candidate models

In [1] a family of related rate-and-state models was introduced, and a systematic attempt was made to discriminate between them based on experimental results. The introduction of a tangential contact stiffness $k_t$ was the key ingredient that allowed these models to capture a number of features in the measurements of $\beta(\omega)$, where earlier models had failed. The physical interpretation of this contact stiffness, and the precise way it was incorporated into the governing equations, was discussed in detail in the earlier work. It is not necessary to repeat that here: suffice it to say that the best fit was obtained with a small subset of the family, and only those cases will be considered in the present work. They are defined here for completeness.

The frictional force $F$ can be expressed by a rate-and-state model that includes the effect of tangential contact stiffness. The two relevant models will be labelled with notation to match the earlier work: the "compliant interface model" (CI) and the "compliant pin model" (CP), respectively. The distinction between them relies on whether the contact stiffness is introduced in the state evolution law or not:

$$\begin{aligned} F &= f(v_0 - \dot{y} - \dot{F}/k_t, \phi) \quad \text{with} \quad \dot{\phi} = -g(v_0 - \dot{y}, \phi)(\text{CI model}) \quad \text{or} \\ \dot{\phi} &= -g(v_0 - \dot{y} - \dot{F}/k_t, \phi)(\text{CP model}) \end{aligned} \tag{4}$$

where $\dot{y}$ is the measured perturbed velocity, $\phi$ is the state variable, and $f$ and $g$ are two functions defining the particular rate-and-state model chosen.

After linearisation and by taking the Fourier transform of Eq. (4), which allows the state evolution law to be solved in the frequency domain, the corresponding frictional frequency response functions can be readily obtained:

$$\beta_{CI}(\omega) = -\frac{g_{,\phi} f'_{ss} + i\omega f_{,v}}{g_{,\phi} + i\omega} \times \frac{1}{1 + i\omega f_{,v}/k_t} \text{ (CI model)} \tag{5}$$

and

$$\beta_{CP}(\omega) = -\frac{g_{,\phi} f'_{ss} + i\omega f_{,v}}{g_{,\phi} + i\omega} \times \frac{1}{1 - i\omega\left[\frac{g_{,\phi} f'_{ss} + i\omega f_{,v}}{(g_{,\phi} + i\omega)k_t}\right]} \text{ (CPmodel)} \tag{6}$$

in which $f'_{ss}$ is the slope of the curve of steady-state frictional force as a function of sliding speed (i.e. the "Stribeck curve"), and $f_{,v}$ and $g_{,\phi}$ are the partial derivatives of the functions $f$ and $g$ with respect to the slip rate $v$ and the state variable $\phi$, respectively. In both cases, the equations are written in a form that shows explicitly the original rate-and-state result (the first term) and the factor by which this must be multiplied to express the effect of contact stiffness (the second term).

The tangential contact stiffness is modelled with a power law of the normal force $N_0$ [39–41]:

$$k_t = \kappa N_0^{\alpha}. \tag{7}$$

Idealised theoretical models suggest a range of possible values for $\alpha$: for a linear spring, $\alpha = 0$; for Hertzian contact, $\alpha = 1/3$; for the Greenwood-Williamson model of rough surfaces, $\alpha = 1$. It is not obvious *a priori* which if any of these models applies to the experimental rig, so $\alpha$ has been kept as a free parameter to be determined by measurement.

Explicit choices for the frictional law and the state evolution law are now needed. It should be emphasised that in the literature of rate-and-state models, these choices have generally been driven by experimental observation and are frequently refined in order to fit new experimental datasets ([18]). This work makes use of the classical Dieterich-Ruina law ([14,15]), which defines the friction force $F$ as

$$F = N_0\mu = N_0[\mu_* + a\ln(v/V_*) + b\ln(\phi/\phi_*)] \tag{8}$$

where $\mu$ is the familiar Coulomb coefficient of friction, $v$ indicates the slip rate at the frictional interface, subscripts * denote chosen reference values of the relevant variables, and $a$ and $b$ are dimensionless model parameters. Eq. (8) needs to be coupled with a state evolution law such as the Dieterich ageing law ([14]) or the Ruina slip law ([15]). In [16] a more generic state evolution law was proposed, that reads

$$\frac{d\phi}{dt} = -\frac{\phi - \phi_{ss}(v, \ldots)}{t_\phi(v, \ldots)} \tag{9}$$

where the subscript $ss$ denotes the steady-sliding value. The time constant $t_\phi$ could be assumed to be a fixed value, or alternatively to be velocity dependent. Eq. (9) can be related to the Dieterich ageing law by assuming $t_\phi \equiv L/v$, where $L$ is the classical constant memory length ([14]), and $\phi_{ss}(v) \equiv L/v$. The latter assumption implies that the reference interfacial state $\phi_*$ is given by $\phi_* = L/V_*$. Both assumptions are consistent with the basic experimental observation that lies behind the Dieterich-Ruina law (8), which states that for steady sliding the coefficient of friction exhibits a logarithmic dependence on the slip rate and can be written as

$$\mu_{ss}(v_0) = \mu_* + (a - b)\ln(v/V_*). \tag{10}$$

**Table 1**
Enhanced rate-and-state models considered in this work.

| Model | Rate-and-state model | | | | Elastic contribution | |
|---|---|---|---|---|---|---|
| | $f'_{ss} = \frac{(a-b)N}{v_0}$ | $f_{,v} = \frac{aN}{v_0}$ | $g_{,\phi} = \frac{v_0}{L}$ | $g_{,\phi} = \frac{1}{t_\phi}$ | $\frac{1}{1 + i\omega f_{,v}/k_t}$ | $\frac{1}{1 - i\omega\left[\frac{g_{,\phi} f'_{ss} + i\omega f_{,v}}{(g_{,\phi} + i\omega)k_t}\right]}$ |
| CI1 | × | × | × | | × | |
| CI2 | × | × | | × | × | |
| CP1 | × | × | × | | | × |
| CP2 | × | × | | × | | × |

Eqs. (8), (10) define the functions $f$ and $g$ respectively. For the purposes of this paper, only the frequency-domain expressions in Eqs. (5), (6) are needed, requiring various partial derivatives of $f$ and $g$. Table 1 lists these quantities for the candidate models to be used here for comparisons with experimental results. The two types of model are listed, model CI and model CP. Each model appears then in two variants (e.g. CI1 and CI2), depending on whether a fixed memory length $L$ or a fixed time constant $t_\phi$ is used. The Table separates the two terms of Eqs. (5), (6): "Rate-and-state model" refers to the first term, "Elastic contribution" to the second. The models to be fitted to the experimental results are obtained from Eqs. (5), (6) by substituting the values from this Table. The set of variables to be identified from a measurement of $\beta(\omega)$ is thus $a$, $b$ and $k_t$, together with either $t_\phi$ or $L$. From a set of $k_t$ values, parameters $\kappa$ and $\alpha$ can then be identified.

There is one more piece of information about the models, which it is useful to show explicitly before starting detailed discussions of parameter-fitting. It concerns the influence of the term $(a-b)$, which characterises the slope $f'_{ss}$ of the steady-sliding friction curve for the Dieterich-Ruina law (10): a positive sign of $(a-b)$ indicates velocity-strengthening behaviour, while a negative sign indicates velocity-weakening behaviour. It is useful to see how the two alternatives influence the form of the frictional frequency response. Fig. 2 shows how the transition from a positive to a negative $(a-b)$ term affects $\beta(\omega)$, in terms of the shape of the Nyquist plot and also the phase variation. In terms of the Nyquist plot, calculated here by using model CI2 (the chosen model parameters are listed in the caption of Fig. 2), the change of behaviour is most evident at lower frequencies. The movement of individual low-frequency values between the different curves is indicated by the dashed grey lines in Fig. 2, which connect corresponding points. As the value of $(a-b)$ changes from positive to negative, the low frequency segments of the Nyquist curves tend to expand within the lower half-plane, crossing into the right half-plane as soon $(a-b)$ becomes negative. This diagnostic behaviour will prove useful later for interpretation of measurements of $\beta(\omega)$.

## 3. Optimising the experimental methodology

### 3.1. Measuring $\beta(\omega)$

In the current work, the experimental database of $\beta(\omega)$ measurements has been enlarged by testing new material combinations. Furthermore, the testing procedure described in [1] has been enhanced to improve the accuracy and robustness of the results, and to allow a consistency check of certain identified model parameter values. The material combinations tested are as follows: polycarbonate pin on glass disc (only a few measurements for this combination were shown in [1]), perspex (PMMA) pin on glass disc, Tufnol pin on glass disc, PTFE pin on glass disc, polycarbonate pin on steel disc, and steel pin on steel disc. For each material combination, efforts were made to collect the dynamic response under different sliding speeds (1–10 mm/s) and for different normal forces (10–60 N). However, as will be explained, not all speed/force combinations proved possible to test with some materials. The data set for the polycarbonate-glass combination will be used in this section to illustrate the new procedure, and results for the other material combinations will be discussed in Section 4.

The post-processing of the recorded data has been improved. All the $\beta(\omega)$ measurements shown in previous works ([36,1]) were contaminated by narrow peaks clearly visible in the investigated frequency range, and particularly prominent with higher sliding speeds. These peaks could disturb the fitting process, distracting the eye and providing a biased identification of the model parameters. A thorough modal-testing campaign on different parts of the rig has been carried out, to track down the origins of these features (which were always assumed to be rig artefacts of some kind). These tests showed that all the significant peaks are indeed associated with natural frequencies of various parts of the measurement rig. At low frequencies, the first lateral and vertical modes of the aluminium frame that holds the loading spring propagate through the measurements. At higher frequencies, modes of the disc come into play. It should be emphasised that rig artefacts of this general kind are inevitable given the contradictory design constraints of this measurement. The rig needs enough flexibility to allow actuation and control of the normal load, but it also needs to be as stiff as possible because the useful frequency range is determined precisely by contamination associated with vibration modes of the structure.

Once these modes have been identified and understood, it is possible to attempt to remove them from the measured frictional frequency response function by pole-fitting and subtraction. It would require further investigation to establish the limits of accuracy of this process, but it gives a very useful first approximation to revealing the underlying physical contact behaviour. Fig. 3 shows the magnitude and Nyquist plots of three $\beta(\omega)$ measurements for the polycarbonate-glass combination, before and after filtering out some of these rig mode artefacts at lower frequencies. The obvious circular features in the Nyquist plots at low frequency disappear without affecting the main circular shape that characterises $\beta(\omega)$ in the complex plane. This modal filtering process has been applied to almost all the experimental data used here.

Fig. 4 shows some of the dynamic friction measurements of the polycarbonate/glass combination taken at fixed normal forces 34 N (Fig. 4a) and 44 N (Fig. 4b), and for different sliding speeds (1–10 mm/s). The pattern shown by magnitude plots of this kind has already been discussed ([36,1]), but it is worth underlining the remarkable repeatability of the $\beta(\omega)$ measurements: each case appears twice, as a solid and a dashed line, but they can scarcely be distinguished in the plot. Not all the investigated material combinations showed such strikingly repeatable behaviour, but it will be argued in Section 4 that this is determined simply by the susceptibility to wear of each material combination.

### 3.2. Sensitivity analysis of the identified model parameters

The parameters of the candidate models are identified through an

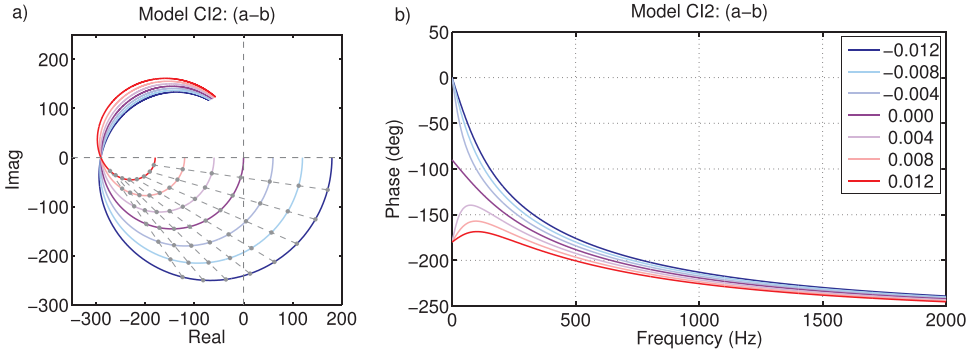


**Fig. 2.** Influence of the $(a-b)$ term on $\beta(\omega)$. Model CI2 has been used to calculate (a) the Nyquist plot and (b) the phase plot over the range 0–2000 Hz. The following parameter values were used: $N_0 = 30$ N, $v_0 = 2$ mm/s, $a = 0.025$, $t_\phi = 0.7$ ms, $k_t = 6 \times N_0^{0.33}$ MN/m. The $(a-b)$ term has been progressively decreased by steps of 0.004, starting from the red curve having a value of 0.012 and ending with the blue curve having a value of 0.012. In Fig. 2a corresponding low-frequency points on each curve have been joined by dashed grey lines, for frequencies 25–200 Hz in steps of 25 Hz. (For interpretation of the references to colour in this figure caption, the reader is referred to the web version of this paper).

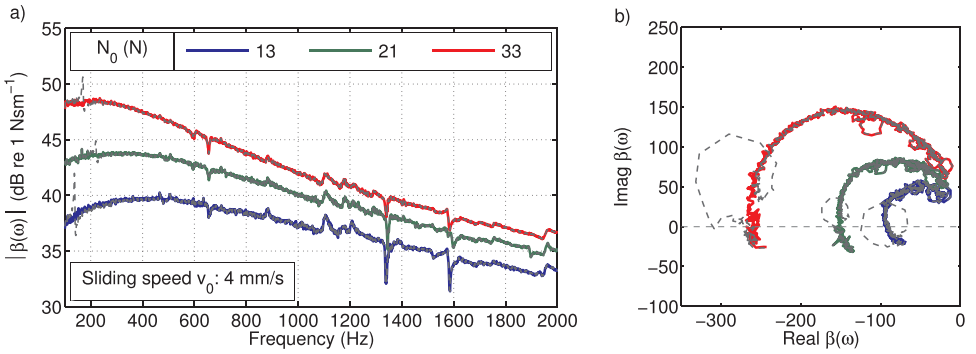


**Fig. 3.** Polycarbonate on glass: a) magnitude and b) Nyquist plot of $\beta(\omega)$ before (grey dashed line) and after (solid line) the modal filtering process. The measurements are referred to a fixed sliding velocity of 4 mm/s and to three different normal forces: 13, 21 and 33 N. (For interpretation of the references to colour in this figure caption, the reader is referred to the web version of this paper).

optimisation process, which minimises a cost function that is the frequency-integrated squared difference between the experimental $\beta(\omega)$ and the corresponding predicted counterpart obtained from Eqs. (5) or (6) (see [1] for more details). It is useful to check the robustness of the identification results. This has been quantified by finding the percentage change in each parameter necessary to increase the cost function by 5% from its minimum value. A high value of this metric, which will be referred to as "high sensitivity", points to the fact that the parameter in question may not be accurately determined by the optimisation process.

Fig. 5 shows the average of this measure of sensitivity for the identified parameters $a$, $b$ and $k_t$ obtained from each candidate model fitted to the individual measurements. (Note that parameters $\kappa$ and $\alpha$ cannot be fitted to individual measurements because they require multiple values of $N_0$: these parameters will be discussed shortly.) Fig. 6 shows a similar averaged plot for the parameters $t_\phi$ and $L$, but in this case the results for models CI and CP are shown separately. There are differences of detail (for example, $b$ is always more sensitive than $a$), but all these parameters show a generically similar pattern of sensitivity: measurements performed at higher speed and lower normal forces, i.e. in the lower right-hand corner of the plots, all show increased sensitivity. This is not unexpected, since measurements in this region usually give low values of $|\beta|$ and hence tend to be more noisy. Parameters $a$, $b$ and $t_\phi$ also show a region of high sensitivity at high normal forces and low speed. The identification of some model parameters in this region is consistently more robust for model CI than for model CP: the maximum change of parameters $t_\phi$ and $L$ seen in Fig. 6a is much lower than in Fig. 6b.

Such sensitivity analysis sometimes reveals situations where certain parameters are not robustly determined by the optimisation approach. Consistency checks of the results are then desirable, and these can sometimes be performed by exploiting alternative types of measurement, as will be explained in the following subsections.

### 3.3. Tangential contact stiffness measurements

A case in point concerns the contact stiffness. In [1] the contact stiffness was simply estimated alongside the other parameters by optimising the fit to the candidate rate-and-state models. However, a straightforward alternative test is possible by running the test rig without rotation of the disc. The measured $\beta(\omega)$ under these conditions should represent the tangential contact stiffness directly: if multiplied by $i\omega$ to convert from force/velocity to force/displacement (i.e. dynamic stiffness), the result would be expected to show a constant value representing the spring stiffness. Fig. 7 shows an example of low-frequency results for a range of normal loads. The excitation bandwidth started at 100 Hz, and above that frequency the expected constant value is seen. Systematic variation with the normal load is also evident. This kind of measurement can easily be incorporated into the standard testing sequence. For the current experimental campaign, a non-sliding test to determine the contact stiffness was carried out before and after each sequence of $\beta(\omega)$ measurements at a given normal force.

There is a possible snag with this method: even with very low forcing amplitude, according to the Cattaneo-Mindlin (CM) assumptions partial interfacial slip should always occur between the two bodies in Hertz-type contact [42,43]. However, tangential sliding during the $\beta(\omega)$ measurements causes wear of a small flat area in the contact region on the pin, accompanied by material transfer. If the non-rotating measurement is made after some sliding tests, the normal pressure distribution and the contact area will have changed, breaking one of the main CM assumptions [44] and allowing the possibility of full sticking with low driving amplitudes. In practice, neither evidence of partial slipping nor a tangential load dependence of the estimated contact stiffness has been observed.

Fig. 8a makes a comparison between contact stiffness values obtained from model optimisation (blue dots) and from non-sliding measurements (red dots). The values are reassuringly consistent. In this particular case the ones identified by the optimisation runs are less widely scattered than the ones obtained from the non-sliding tests, so perhaps the optimisation results are more reliable, but this will not be

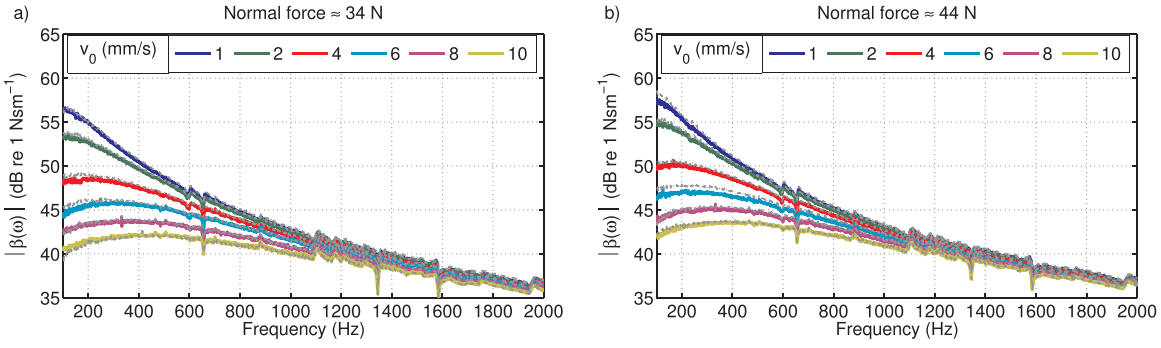


**Fig. 4.** Polycarbonate on glass: magnitude plots of the $\beta(\omega)$ measurements for different sliding speeds (1–10 mm/s) at fixed normal forces (a) 34 N and (b) 44 N. The dash-dot grey lines show the repeatability of the measurement. (For interpretation of the references to colour in this figure caption, the reader is referred to the web version of this paper).

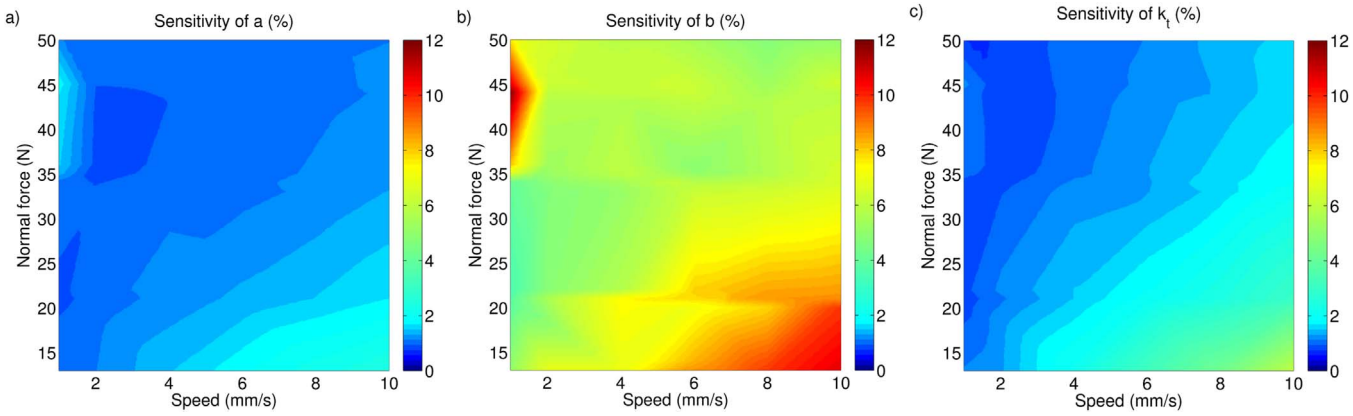


**Fig. 5.** Polycarbonate on glass: averaged sensitivity coefficients obtained from the identified model parameters optimising the four candidate models (see Table 1): a) parameter $a$; b) parameter $b$; c) contact stiffnes $k_t$. The colour scale represents the same percentage range in each case, describing the proportional change in value needed to increase the cost function by 5% from the minimum value. (For interpretation of the references to colour in this figure caption, the reader is referred to the web version of this paper).

the case with all later tests. A remark can be made about the repeatability of the results over the various tests done at different normal forces: in this case the contact stiffness seems to show similar values for each narrow cluster of normal forces, and it can be concluded that the tests done on this material combination are not confused by significant wear effects. Again, this will not be the case for some tests with other materials.

Fig. 8b gathers the stiffness values obtained from the optimisation method into a 3D surface plot against sliding speed and normal force. The power law from Eq. (7) gives a good fit (transparent surface), with values $\varkappa = 3.5 \times 10^5$ N/m and $\alpha = 0.265$.

### 3.4. Steady-sliding curves

According to the Dieterich-Ruina law for the steady-sliding case, Eq. (10), the derivative with respect to velocity of the steady-sliding friction force, $f'_{ss}$, is proportional to the difference $(a - b)$. The values of the parameters $a$ and $b$ obtained by comparing the rate-and-state models with the $\beta(\omega)$ measurements can thus be cross-checked by fitting Eq. (10) to the measured steady-sliding coefficient of friction. The friction coefficient $\mu_{ss}$ has been estimated alongside each measurement of $\beta(\omega)$, tested using different velocities and normal forces: the results are plotted in Fig. 9a. The parameters of the Dieterich-Ruina law have been estimated by optimising the fit of Eq. (10) to each measured set of $\mu_{ss}$. These parameters can then be used to compute the derivative with respect to velocity of $\mu_{ss}$. The same quantity can be calculated using the values of $a$ and $b$ fitted from the $\beta(\omega)$ measurements. Fig. 9b plots a comparison, showing fairly good agreement between the estimated $\partial\mu_{ss}/\partial v$ obtained by the two approaches.

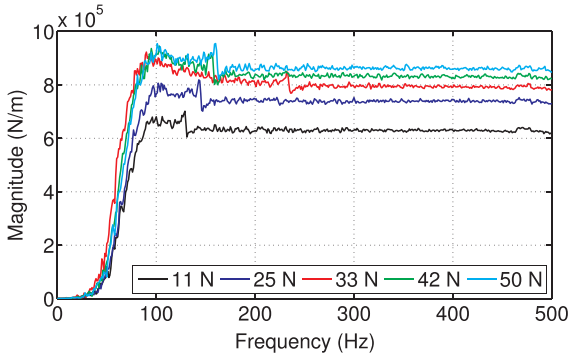


**Fig. 7.** Polycarbonate on glass: examples of non-sliding measurements of dynamic stiffness for different normal forces. (For interpretation of the references to colour in this figure caption, the reader is referred to the web version of this paper).

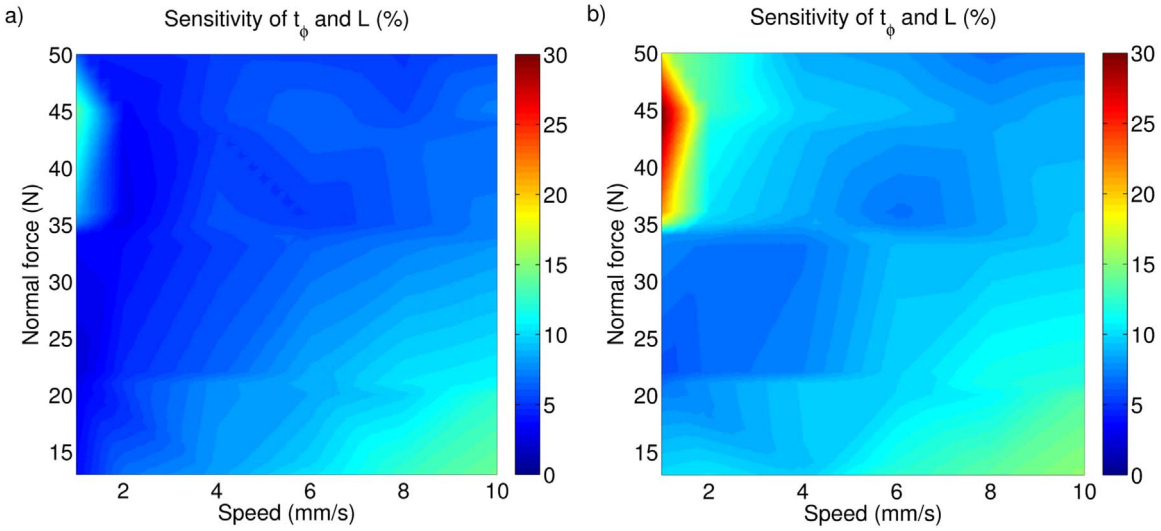


**Fig. 6.** Polycarbonate on glass: averaged sensitivity coefficients for the identified parameters $t_\phi$ and $L$ obtained by optimising a) model CI1 and CI2; b) model CP1 and CP2. The colour scale represents the same percentage range in each case, but a different range from that in Fig. 5. (For interpretation of the references to colour in this figure caption, the reader is referred to the web version of this paper).

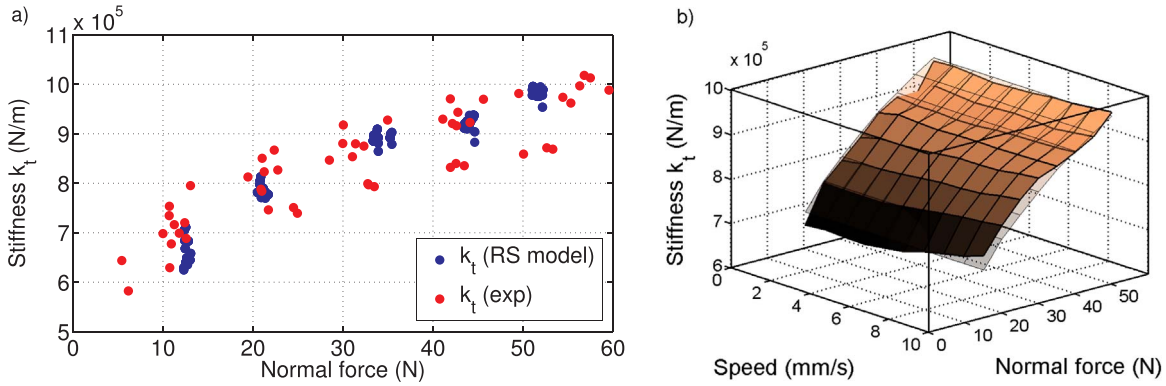


**Fig. 8.** Polycarbonate on glass: a) comparison of the contact stiffness $k_t$ identified from non-sliding pin-on-disc measurements (red dots) and model optimisation runs (blue dots); b) a power law fit (transparent surface) to the stiffness values obtained from the optimisation run. (For interpretation of the references to colour in this figure caption, the reader is referred to the web version of this paper).

### 3.5. Data matrix fitting

The two consistency checks just described have two main applications:

1. they allow cross-checking of the model parameters identified by optimisation runs based on $\beta(\omega)$, which can sometimes lead to unreliable numerical results if a large number of fitting parameters are involved;
2. if a sensitivity analysis highlights a model parameter for which identification is not robust enough, it may be possible to eliminate that parameter from the optimisation procedure by identifying it first through an alternative measurement.

The case shown so far, for polycarbonate on glass, showed quite robust behaviour for all fitting parameters. The most sensitive one seemed to be the time- or length-scale of the state variable, $t_\phi$ or $L$, for which an alternative test has not yet been implemented. On the other hand, some other material combinations — such as the perspex (PMMA) pin on glass disc — exhibit a stronger sensitivity for $t_\phi$ or $L$ and for the parameter $b$, as will be discussed in Section 4. To fit the full data matrix for the polycarbonate on glass case, three fitting parameters have been chosen: $a$, $b$, and $t_\phi$ or $L$. The contact stiffness was kept fixed with the power law identified in Section 3.3, since Fig. 8 showed a very consistent pattern of the identified stiffness values for different normal forces and sliding speeds.

In order to discriminate among the four rate-and-state candidate models, each model was independently fitted to the 60 measured $\beta(\omega)$ curves. The parameters obtained from each fitted curve were then used to run simulations in order to predict the whole data matrix. Fig. 10 shows the estimates of the normalised Schwartz Bayesian Information Criterion (SBIC), as used previously in [1]. This index quantifies the goodness of fit per simulation ([45]): lower SBIC values indicate more favoured models. The plots was produced using the Matlab function "*boxplot*". The ends of the rectangles show the 25th and 75th percentiles of the distribution, and the central lines indicate the median. Outliers are indicated by the isolated dots. Among the four candidate models it is evident that model CI2 performs the best, meaning that it is better able to catch the full pattern of the experimental data.

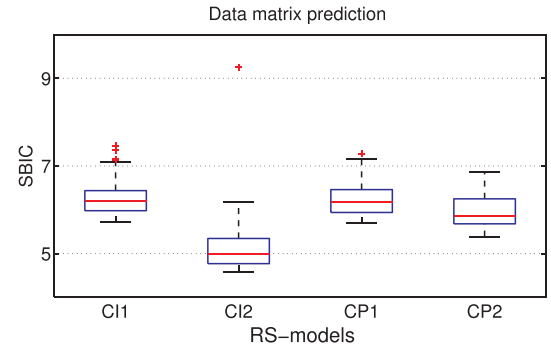


**Fig. 10.** Polycarbonate on glass: estimation of the accuracy of full data matrix prediction by using single sets of fitted model parameters, based on the Schwartz Bayesian Information Criterion. The central horizontal line indicates the median of the different SBIC values, the rectangle box defines the 25th and 75th percentiles of the data distribution and the outliers are marked as red dots. (For interpretation of the references to colour in this figure caption, the reader is referred to the web version of this paper.)

Histograms of the 60 identified values of $a$, $b$ and $t_\phi$ from model CI2 are shown in Figs. 11a and b. The values of $a$ are consistently higher

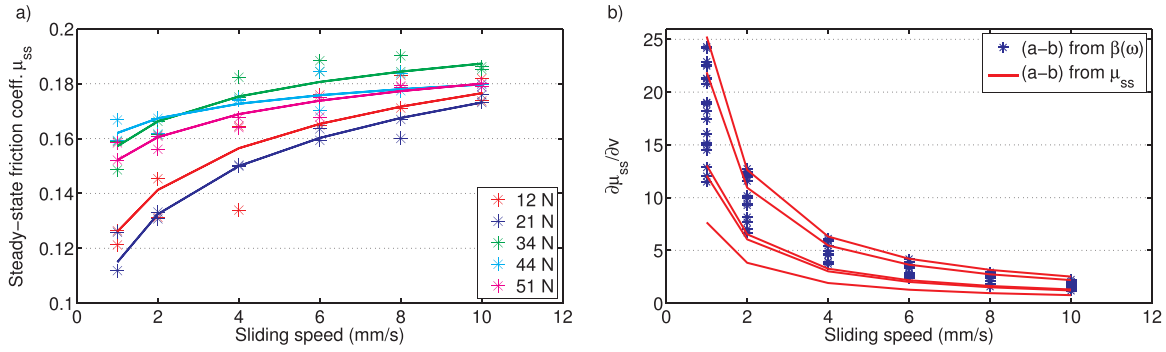


**Fig. 9.** Polycarbonate on glass: a) steady-sliding coefficient of friction $\mu_{ss}$ measured for different normal forces and sliding speeds. The solid lines are the fitted Dieterich-Ruina laws obtained for each set of $\mu_{ss}$; b) comparison of the derivative with respect to velocity of $\mu_{ss}$ obtained from equation (10), using the fitted Dieterich-Ruina law (red lines) and using the fitted $\beta(\omega)$ models, CI and CP (blue stars). Note that there are 10 blue stars for each sliding speed, because each speed was tested twice with given normal force. (For interpretation of the references to colour in this figure caption, the reader is referred to the web version of this paper).

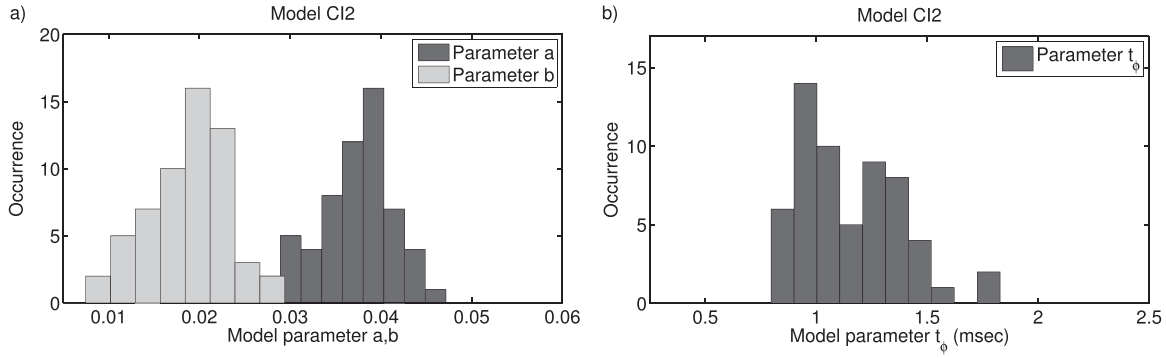


**Fig. 11.** Polycarbonate on glass: a) histogram of the identified model parameters $a$ and $b$ obtained from model CI2; b) histogram of the identified model parameter $t_\phi$ obtained from model CI2.

than those of $b$, which agrees with the observed pattern of the steady-sliding data, and both values show a confined and normal distribution around mean values of 0.037 and 0.018, respectively. On the other hand, the state variable time-scale $t_\phi$ shows a quasi-uniform variation between 0.8–1.5 msec, with a mean value of 1.1 msec. A few values are higher than 1.5 msec, but these come from $\beta(\omega)$ measured at low speeds and high normal forces, and it has already been seen in Fig. 6a that these values in the top left corner of the plotted matrix are subject to a high degree of uncertainty.

Figs. 12a–e show Nyquist plots for different subsets of these measurements. The blue dashed lines show the results obtained by fitting model CI2 to each single $\beta(\omega)$ curve separately. The chosen rate-and-state model, including the stiffness term, is able to give an excellent match to each single experimental curve over the entire range of sliding speeds and normal forces. The solid red curves show the result of the best fit to the whole experimental data matrix with a single set of model parameters: model CI2 with the parameter values $a = 0.037$, $b = 0.017$ and $t_\phi = 1.2$ msec. These best-fitted parameters are very close to the mean values of the distributions shown in Fig. 11. The results show a reasonably good fit over the whole range of normal force, sliding speed and frequency; although of course they are usually not quite as good as the individual fits.

## 4. Tests with other material combinations

### 4.1. Overview

The main aim of this paper is to explore how widely the models advocated in the earlier study can be applied. The individual discussions of separate material combination will necessarily be quite

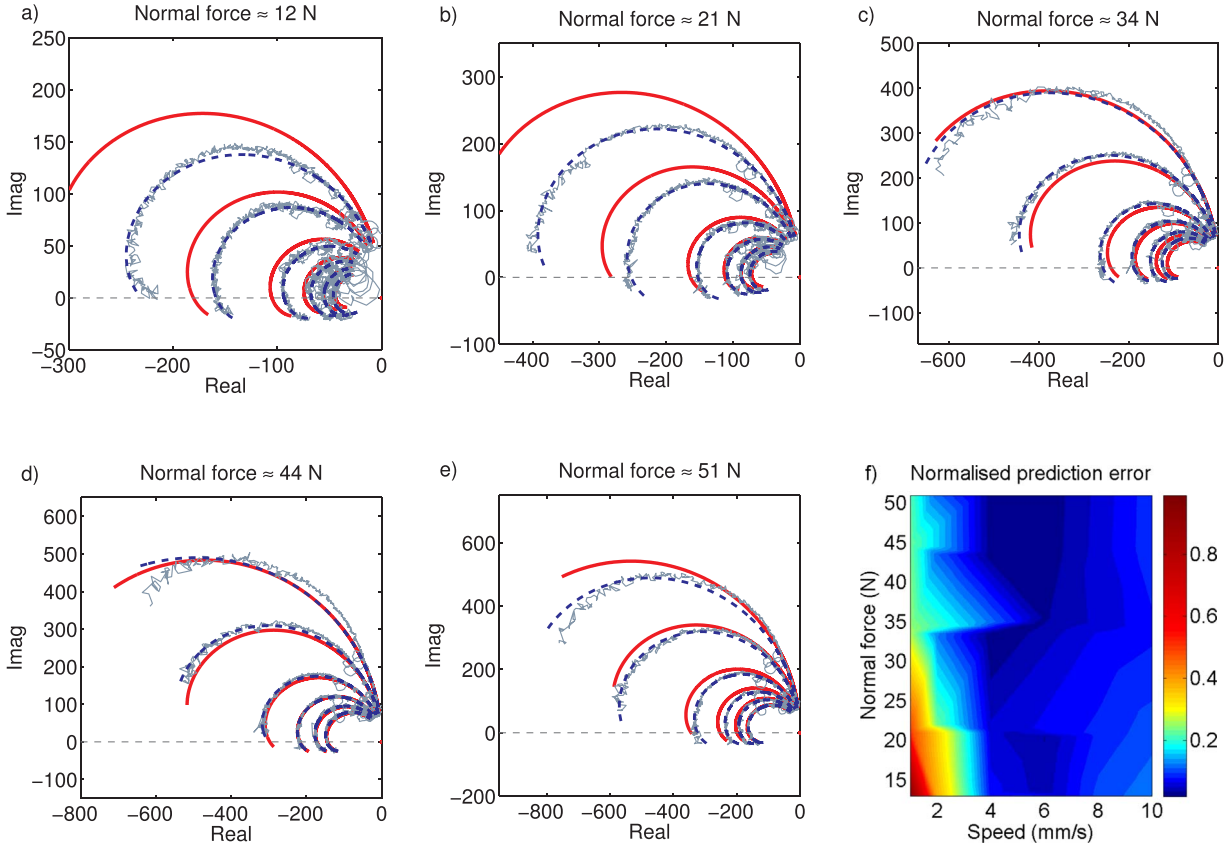


**Fig. 12.** Polycarbonate on glass: comparison between model CI2 and $\beta(\omega)$ measurements. Dashed blue lines represent best fits to each single curve, solid red lines relate to global fitting of the whole data matrix. Fig. 12f shows the prediction error obtained for each curve by fitting the whole data matrix, normalised by dividing by the maximum value. (For interpretation of the references to colour in this figure caption, the reader is referred to the web version of this paper).

detailed, so before embarking on that it is important to give an overview of similarities and differences among the materials. Later subsections discuss the main results obtained by testing pins of different materials against a glass and a steel disc. The choice of these particular material combinations was not motivated by any specific engineering application, although some of the tested materials are of industrial importance, for example PTFE in self-lubricating bearing materials. The intention was simply to explore the behaviour of $\beta(\omega)$ over a range of materials that were conveniently available in a suitable form for the test rig.

As already anticipated in Section 3, some of the material combinations show the same high level of repeatability as the $\beta(\omega)$ measurements already highlighted by polycarbonate on glass (see previous section) and nylon on glass (see [1]). Perspex (PMMA) on glass performed well in this regard, and Tufnol on glass performed moderately well. However, repeatability is dependent on the chosen operational conditions. Tests shown here used a range of sliding speeds between 1–10 mm/s and normal forces between 10–60 N. Tests at significantly higher speeds or higher normal forces would be likely to induce significant wear, and if the contact conditions are changing, the $\beta(\omega)$ measurement would be expected to change too. This has already been shown for the case of polycarbonate on glass, reported in [1], and it became much more intrusive when a PTFE pin was tested against glass. The wear was now so rapid that the contact conditions changed significantly during each series of runs, and the results were much less repeatable than those seen so far. Details will be shown in Section 4.5.

After showing some examples of these results for polymeric pins against glass, a few results are shown using a steel disc. For direct comparison, results are shown for polycarbonate on steel, then finally some results are shown for a steel pin against the steel disc. For the polycarbonate pin, the issue of wear was again important. Probably because of the higher level of surface roughness of the steel disc compared to the glass one, the wear rate was higher and after a certain period of testing the pin started to generate squeal. The steel pin, however, showed good repeatability as will be illustrated in Section 4.7

All these comments about wear were verified directly by examining pins in the scanning electron microscope, before and after testing. A typical example of the results is shown in Fig. 13, which shows a polycarbonate pin before and after testing on the steel disc. The machining marks are clearly visible in the “before” image, but after testing these marks have been obliterated and a large flat area created: in this case it is over 1 mm in diameter.

### 4.2. Summary of identified model parameters: polymers

This section presents a summary of the identified model parameters $a$, $b$, $t_\phi$ or $L$, and the contact stiffness coefficients $\kappa$ and $\alpha$. The model parameters have been identified by following the experimental methodology described above:

1. measure $\beta(\omega)$, together with $\mu_{ss}$ and the contact stiffness from tests without disc rotation;
2. perform a sensitivity analysis for each model parameter of the candidate friction models, identify any fitting parameters that show a high sensitivity, then identify such parameters through alternative friction tests and fix them during the optimisation process;
3. discriminate among the candidate friction models by fitting each model independently to the measured $\beta(\omega)$ curves, then use the parameters obtained from each fitted curve to run simulations in order to predict the whole data matrix, or for cases where the material combination was significantly affected by wear, chosen subsets of the matrix.

Table 2 summarises the selected model for each tested material combination, including for completeness the case of nylon on glass explored in [1]. Apart from the polycarbonate on steel case, the best match with the experimental curves was always provided by the rate-and-state model containing the elastic contribution within the friction law (models CI*n*), rather than in the state-evolution law (models CP*n*). For nylon/glass, polycarbonate/glass, perspex/glass and Tufnol/glass, the differences in terms of fitting error between models CI*n* and models CP*n*, used to fit each data matrix, was always at least 30%. A further discriminating factor consisted in the choice of fixed time-scale or fixed length-scale for the state variable evolution law. It was found that in order to allow the whole data matrix to be fitted, for some cases a fixed time-scale $t_\phi$ worked best, while for other cases a fixed length-scale $L$ was better. There is no clear physical reason for either model to be fully accurate, and it may turn out that a different assumption will be needed. Alternative friction tests to give an independent way to probe the behaviour of the state variable are still under investigation, and not yet implemented here. For the Tufnol on glass case, it was found that one subset of data collected at a high normal force worked best with model CI1, whereas the other tests worked better with model CI2. For the subset at a high normal force, the fitting error provided by model CI1 was one order of magnitude lower than the fitting error obtained by using model CI2. The fitting of the PTFE/glass case was only possible with the CI1 model. This material combination pushed the whole fitting methodology to its limit.

Figs. 14a and b summarise the distributions of the identified values of model parameters $a$, $b$ and $t_\phi$ for each material combination. The model parameters are referred to the models highlighted in Table 2. The broad similarity of parameters $a$ and $b$ across these disparate materials is quite striking. The histograms show similar normal distributions for the nylon, polycarbonate and perspex (PMMA) on glass cases. The data matrix of each of these material sets can be predicted quite well by a single set of model parameters, with values close to the mean value of each distribution. The identified parameters of the remaining material combinations show a more uniform and widely-scattered distribution, and only single experimental curves or subsets of the data matrix can be

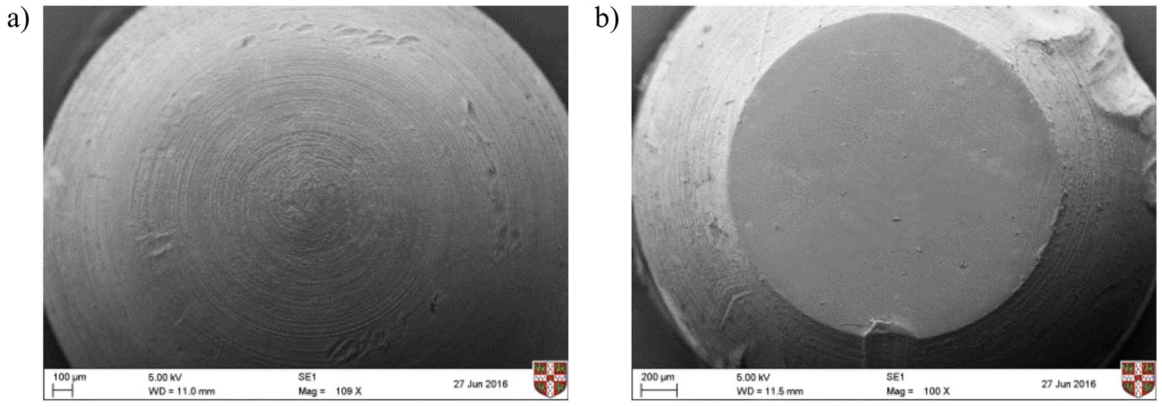


**Fig. 13.** Scanning electron microscope images of a polycarbonate pin used against the steel disc: a) new sample; b) sample after several sequences of testing.

**Table 2**
Selected rate-and-state model for each material combination.

| Nylon–Glass | Polycarbonate–Glass | Perspex-Glass | Tufnol–Glass | PTFE–Glass | Polycarbonate–Steel |
|---|---|---|---|---|---|
| CI2 | CI2 | CI2 | CI1/CI2 | CI1 | CP1 |

fitted by any particular selected model. The histograms also show that parameter $a$ is always larger than parameter $b$, although some material combinations — especially polycarbonate on steel — give a smaller difference $(a - b)$. This will be discussed in some detail in subsequent sections.

Fig. 14b shows narrow distributions of the identified values of $t_\phi$ for the nylon-glass, polycarbonate-glass and polycarbonate-steel cases. For the first two of these, the time-scale $t_\phi$ ranges between 0.5–1.8 msec, while for the latter material set it appears to be lower than 0.6 msec. However, the remained polymer cases show values of $t_\phi$ that are much more widely scattered. Note that for model CI1 and CP1, the values of $t_\phi$ have been inferred from $L/v$.

As discussed in Section 3.3, the contact stiffness can be determined by fitting a power law to the identified values of $k_t$ obtained either from the optimisation runs performed at different normal forces, or by running the test rig while keeping the disc still. The latter option has been adopted for the PMMA-glass and Tufnol-glass cases, since it provided less scattered values of contact stiffness. Fig. 15 summarises the fitted values of $\kappa$ and $\alpha$ from Eq. (7). For the four material combinations for which the data was good enough to allow convincing global fitting a single symbol (cross + circle) is plotted.

However, for the material combinations that were prone to rapid wear, it was not possible to fit a single power law since the contact stiffness kept changing after each sequence of runs. Therefore, parameter $k_t$ was either kept as a fitting parameter during each individual optimisation run (polycarbonate on steel), or different power laws were fitted to different subsets of the contact stiffness measurements (PTFE on glass). For both material combinations, Fig. 16 shows the contact stiffness values estimated from the "direct" measurement. Each coloured series of dots refers to the contact stiffness estimated before and after a full sequence of $\beta(\omega)$ measurements performed at a fixed normal force. It can be observed that the contact stiffness tends to increase after each sequence of measurements. Each line was then separately fitted to Eq. (7), and the results are plotted in Fig. 15 with star and diamond markers respectively.

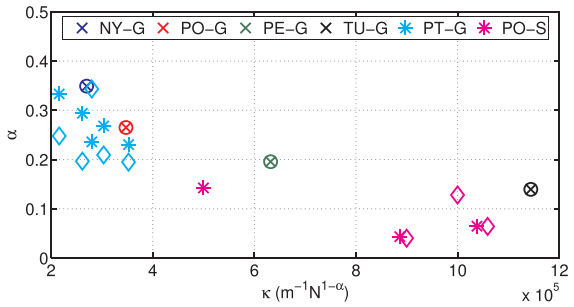


**Fig. 15.** Identified values for $\kappa$ and $\alpha$ for the different material combinations. Different pairs of $\kappa$ and $\alpha$ have been fitted to subsets of the PTFE on glass and the polycarbonate on steel cases, because of wear issues: see main text and Fig. 16. The star and diamond symbols refer to the contact stiffness estimated before and after a full sequence of $\beta(\omega)$ measurements, respectively. (For interpretation of the references to colour in this figure caption, the reader is referred to the web version of this paper).

### 4.3. Perspex (PMMA) on glass

Perspex on glass has been tested for the full range of sliding speeds (1–10 mm/s) and normal forces (12, 21, 35, 50, and 61 N), measuring $\beta(\omega)$ and $\mu_{ss}$. Wear effects were not of particular concern, and all the measurements exhibited good repeatability.

Sensitivity analysis revealed parameter $b$ to be particular sensitive: Fig. 17a shows that generally the sensitivity coefficient is around 20%, while a small area within the data matrix shows values up to 90%. The main cause of such low robustness of the optimisation seems to be a smaller value of $(a - b)$, sometimes producing misleading identification results with $a$ lower than $b$. To overcome such problems, $(a - b)$ was estimated by fitting the Dieterich-Ruina law (8) to the measured $\mu_{ss}$ (Fig. 17b). Fig. 17b shows $\mu_{ss}$ only increasing slowly as the sliding speed is increased, directly suggesting a low but positive value of $(a - b)$.

The values of $(a - b)$ and the contact stiffness (see Fig. 15) were then fixed, and the optimisation process re-run with only two fitting parameters: $a$ and $t_\phi$. First each separate $\beta(\omega)$ measurement and then

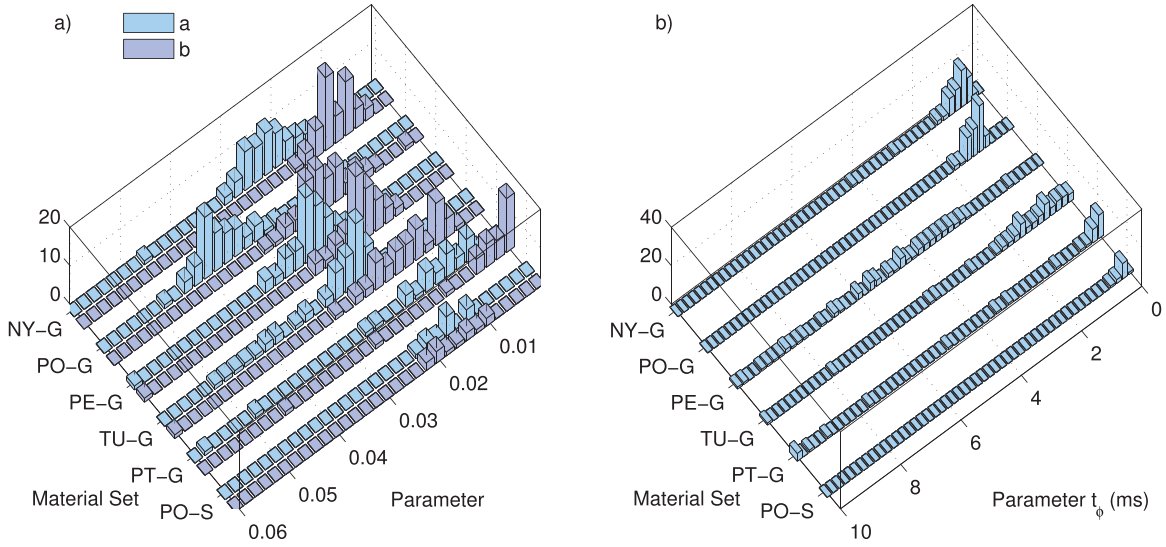


**Fig. 14.** Histogram distributions of the identified values of model parameters for each material combination: a) $a$ and $b$; b) $t_\phi$. (For interpretation of the references to colour in this figure caption, the reader is referred to the web version of this paper).

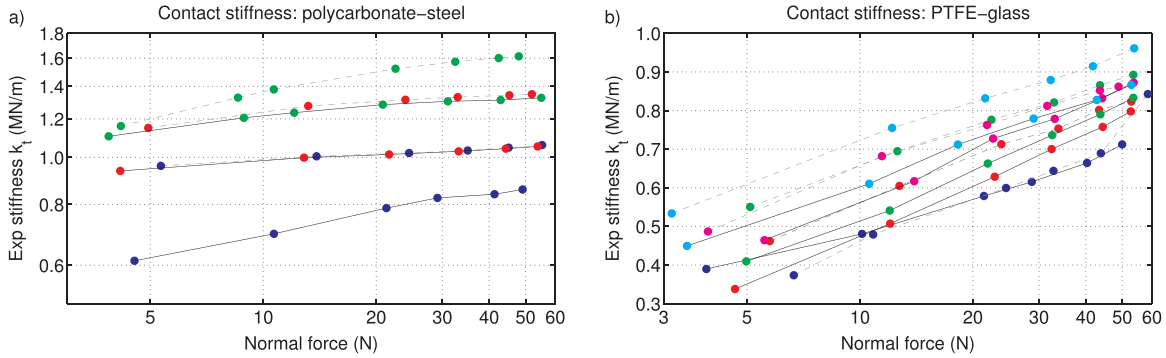


**Fig. 16.** Estimated values of contact stiffness obtained by running the test rig without disc rotation: a) polycarbonate on steel; b) PTFE on glass. For (a), the blue, red and green dots indicate measurements performed before and after a sequence of $\beta(\omega)$ measurements performed around 10 N, 25 N and 37 N, respectively. For (b), the blue, red, green, magenta and cyan dots indicate measurements performed before and after a sequence of $\beta(\omega)$ measurements performed around 12 N, 21 N, 31 N, 43 N and 50 N, respectively. (For interpretation of the references to colour in this figure caption, the reader is referred to the web version of this paper).

the whole data matrix was fitted using model CI2. Fig. 18a shows a typical sequence of $\beta(\omega)$ measured at a fixed normal force ($\approx$ 50 N), while Fig. 18b provides an example of the fitting results in a similar format to Fig. 12. The magnitude plots of $\beta(\omega)$ in Fig. 18a clearly demonstrate the remarkable level of repeatability over all the runs between 1–10 mm/s: the dashed grey lines are scarcely detectable due to almost perfect matching.

As already discussed in Section 3, whenever the different measurements of $\beta(\omega)$ exhibit good repeatability, it has been possible to predict the collected experimental data matrix by using a single set of model parameters. This was the case for the PMMA on glass material set. The solid red lines in Fig. 18b refer to the global fit obtained by using model CI2. The fitted parameters are: $a = 0.0237$, $b = 0.0155$ and $t_\phi = 3.5$ ms. In general, both individual and global fits, blue dashed lines and red solid lines in Fig. 18b respectively, reproduce the variation of $\beta(\omega)$ quite well over the entire range of sliding speeds, normal forces and frequencies.

### 4.4. Tufnol on glass

The results for Tufnol on glass tell a slightly more complicated story. The $\beta(\omega)$ measurements still show excellent repeatability, as illustrated in Fig. 19 showing the real and imaginary parts of $\beta(\omega)$ measured for different sliding speeds (1–10 mm/s) with a fixed normal force ($\approx$ 22 N). The dashed grey lines are always very close to the coloured lines.

The first striking result concerns the measured $\mu_{ss}$. Fig. 20a shows the coefficients of friction measured by varying the sliding speed between 1–10 mm/s at different fixed normal forces: 12, 22, 33, 44 and 60 N. Conversely, the friction force is plotted against the normal force in Fig. 20b for different values of sliding speed. By inspecting both Figs. 20a and b, several trends can be discerned. The first three sequences of measurements, done between 12–33 N, seem to obey Coulomb's law and also to show a slight but consistent velocity strengthening behaviour. The measurements done at 60 N exhibit a rather constant value of $\mu_{ss}$ during the first set of tests with increasing sliding speed, fluctuating around 0.25, but then during the second set of tests as sliding speed was reduced they show a steady and significant increase up to 0.35. An intermediate pattern is shown by the measurements performed at 44 N. In addition, the measurements performed at 44 and 60 N seem to deviate increasingly from Coulomb's law.

Inspecting the measured $\beta(\omega)$ for different normal forces reveals a second striking result. Fig. 21 shows that for the measurements performed at 12 N and 60 N, the Nyquist plots exhibit an extension into the lower half-plane at low frequency, while all the other Nyquist plots are predominantly confined to the upper half-plane and also show a more consistent pattern of behaviour. This discrepancy meant that it was not possible to predict the whole data matrix by a rate-and-state model using a single set of parameters, even though each individual curve could still be fitted very well. The sensitivity analysis revealed that the contact stiffness parameter was not determined very robustly, especially for high speeds and low normal forces, so the "direct" measurement of contact stiffness was exploited to identify $\kappa$ and $\alpha$ (see Fig. 15), then both parameters were fixed during the optimisation runs.

A slightly different approach was needed in order to discriminate among the candidate models in this case. After fitting the different $\beta(\omega)$ curves independently with each model, the resulting set of identified model parameters were used to predict only the subset of the data matrix measured at the same normal force as the fitted $\beta(\omega)$. For most of the data set the most suitable model proved to be CI2, but model CI1 seemed preferable for the subset of data recorded at 60 N. Recall that the only distinction between these models is the use of a fixed time-scale in CI2, versus a fixed length-scale in model CI1.

The blue dashed lines in Fig. 21 show the individual fit for each $\beta(\omega)$ measurement: they clearly show an excellent match with the experimental curves in all cases. The solid red lines refer now to the fit performed on the subsets of data measured at a fixed normal force. Apart from the measurements performed at low sliding speeds and low normal forces (Fig. 21a), the "subset" fit seems to catch quite well the

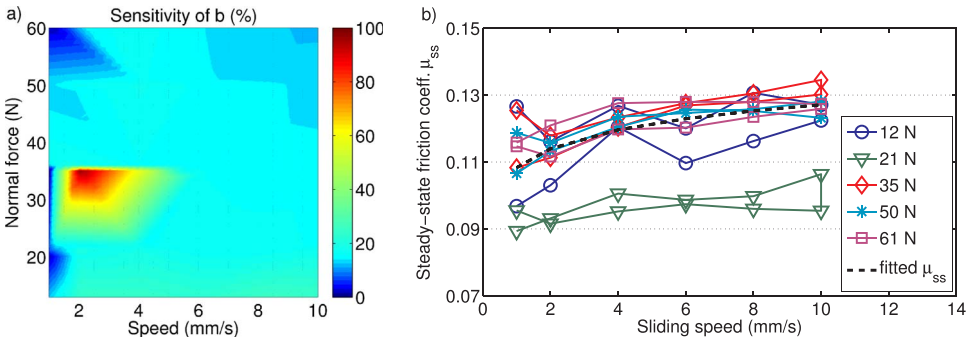


**Fig. 17.** Perspex (PMMA) on glass: a) sensitivity analysis of parameter $b$; b) steady-state coefficient of friction $\mu_{ss}$ and fitted Dieterich-Ruina law (black dashed line). (For interpretation of the references to colour in this figure caption, the reader is referred to the web version of this paper).

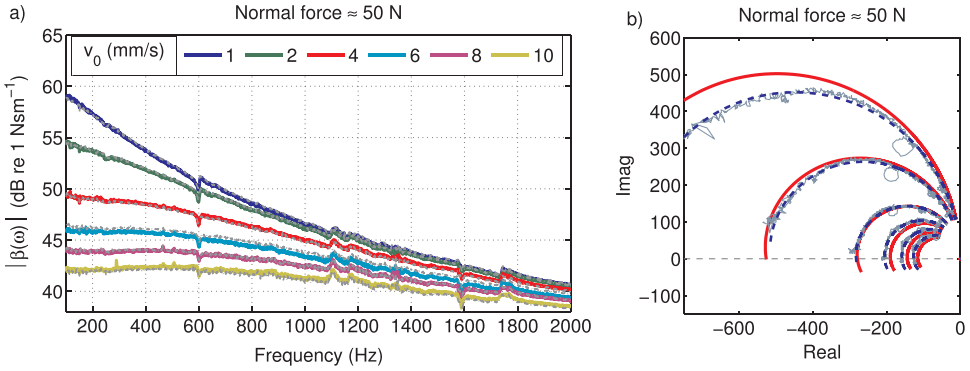


**Fig. 18.** Perspex on glass: a) magnitude plots of $\beta(\omega)$ measured twice at a range of different sliding speeds (1–10 mm/s); b) fitting results obtained by using model CI2, for the experimental data shown in Fig. 18a. The blue dashed line corresponds to an individual fit, while the red solid line is related to the fit of the whole data matrix. (For interpretation of the references to colour in this figure caption, the reader is referred to the web version of this paper).

variation of $\beta(\omega)$ for different sliding speeds and frequencies. A further remark can be made about the fitting performance of models CI2 and CI1 for the subset of data measured at 60 N, Figs. 21e and f respectively. A systematic difference can be seen at lower frequencies, where the plot lies in the lower half-plane: model CI1 seems to catch the downward extension of the $\beta(\omega)$ measurements rather better.

Table 3 summarises the identified model parameters for each "subset" fit. It can clearly be seen that the data measured between 22 and 44 N could have been fitted by one single set of model parameters, since the tabulated values of $a$, $b$ and $t_\phi$ are all quite similar. On other hand, the first and fifth columns show significantly different values of model parameters. Finally, the last column concerning model CI1 shows the values of $a$ and $b$ being almost equal. This is consistent with what was seen in the $\mu_{ss}$ plot in Fig. 20b: the first sequence of the $\mu_{ss}$ measured at 60 N seems to be quite independent of the sliding speed, requiring a very small value of $(a - b)$ in the Dieterich-Ruina law (10).

### 4.5. PTFE on glass

For the PTFE-glass combination, $\beta(\omega)$ was measured for a range of sliding speeds between 1–10 mm/s and normal forces of 12, 21, 31, 44 and 52 N. Fig. 22a shows an example set of measurements, for different sliding speeds at a normal force around 31 N. This time the grey dashed lines do not match the coloured lines exactly, and the discrepancy becomes more evident at higher sliding speeds. As already anticipated in Section 4.2, the results for this material combination were significantly influenced by wear effects. However, even for this case the repeatability is moderately good when set against typical traditional measurements of friction. Compared to previous material sets, the measurements of $\beta(\omega)$ were also characterised by a higher noise level, which made the optimisation runs less straightforward.

In order to keep the number of fitting parameters low, different values of $\kappa$ and $\alpha$ were identified for each subset of data measured at a fixed normal force, by exploiting the "direct" measurement of the contact stiffness (see Figs. 15– Figs. 16b). The fitting parameters were then $a$, $b$ and $L$, and the most suitable model was found to be CI1. Fig. 22b shows an example of the fitting results, in which only individual fits are shown. For this particular material combination, occasional results produced poor fits or unreasonable model parameters (e.g. high values or $a < b$): one such has been excluded from the plot.

As one would expect for PTFE, the measurements of $\mu_{ss}$ gave very low values, varying between 0.02 and 0.15. The friction force was found to obey Coulomb's law only for normal forces up to 30 N. The observed deviations at higher normal force were again presumably attributable to rapid wear.

### 4.6. Polycarbonate on steel

Polycarbonate on steel proved to be one of the most interesting case studies since the measurements of $\beta(\omega)$ were characterised by a repeatable transition between the desired perturbed sliding condition and squeal occurrence. Only three sequences of runs were performed, since the pin sample wore rapidly at higher normal forces. During each sequence the sliding speed was varied between 1–10 mm/s. The mean levels of the normal forces for the three sequences were 11, 23 and 36 N, respectively. The wear process led to variations between ± 7–30 %. The effect of wear is clearly visible in Fig. 23a: for example the points marked with arrows show the first and last run for the sequence of tests performed around 23 N. This plot also suggests that for all sliding speeds Coulomb's law still holds.

Fig. 23b shows the estimated $\mu_{ss}$ coefficients, and also indicates the cases when squeal was observed. For the runs performed at 23 and 36 N the effect started at a sliding speed of 6 mm/s, persisted for higher velocities and ceased only when the sliding speed was decreased again beyond 6 mm/s. For the runs performed at 11 N, squeal was detected only at a sliding speed of 6 mm/s. In all cases the squeal was intermittent but clearly audible, and occurred in the vicinity of 5 kHz.

All the measured $\mu_{ss}$ values tend to increase with increasing sliding speed. However, in the second half of each series of tests with the velocity decreasing, the friction coefficients tend to settle around an

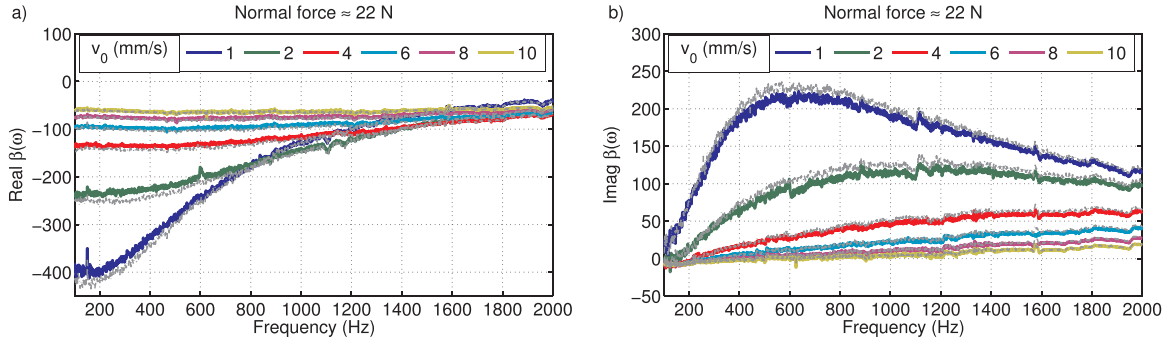


**Fig. 19.** Tufnol on glass: $\beta(\omega)$ measured twice at a range of different sliding speeds (1–10 mm/s) and at a fixed normal force (≈ 22 N): a) real part; b) imaginary part. (For interpretation of the references to colour in this figure caption, the reader is referred to the web version of this paper).

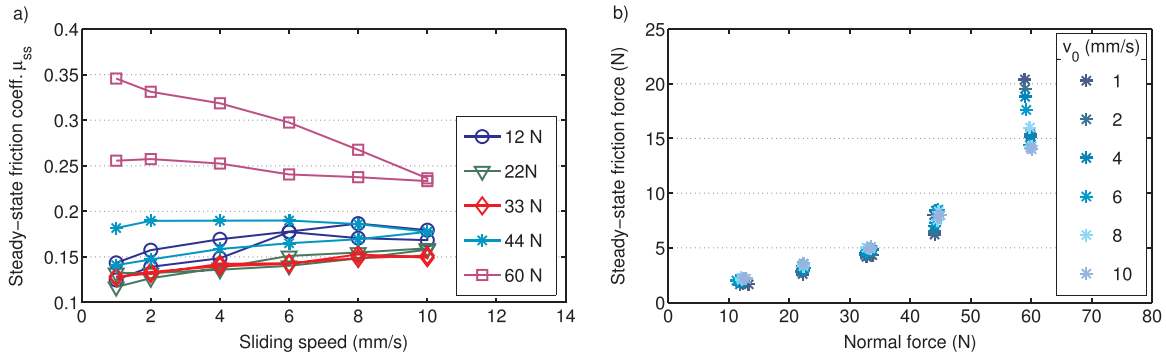


**Fig. 20.** Tufnol on glass: a) measurements of $\mu_{ss}$ for different sliding speeds and normal forces; b) friction force against normal force plotted for different sliding speeds. (For interpretation of the references to colour in this figure caption, the reader is referred to the web version of this paper).

approximately constant value. A curious feature of these results is the remarkably consistent starting point for each sequence of runs: although the surface of the pin is affected by wear during each run (see Fig. 13), each sequence of measurements starts at a value of $\mu_{ss} \approx 0.4$. Perhaps another factor such as temperature is also playing a role, but at present the explanation is unknown.

Bearing in mind that squeal affected most of the data, only $\beta(\omega)$ measurements at 1 and 2 mm/s during each sequence of runs have been used for the model discrimination analysis. The sensitivity analysis of the identified model parameters provided quite robust values (<7%), with the biggest deviation appearing for the data measured at a low normal force, as already observed in previous cases. In order to discriminate among the models, a similar strategy was adopted to that used for the Tufnol on glass case. However, since the measured $\beta(\omega)$ showed slight differences after a couple of runs, the model parameters identified for each $\beta(\omega)$ curve have been used to predict only the curve at the other sliding speed measured for the same normal force. In addition, the contact stiffness $k_t$ was kept as a fitting parameter for each run. Model CP1 was identified as the most suitable model (see Table 2).

Fig. 24 illustrates the fitting performance related to the first two $\beta(\omega)$ curves for each subset of data. The dashed blue line corresponds to an individual fit, while the solid red line to the "subset" fit. Both agree remarkably well with the experimental data. The first three columns of Table 4 show the identified model parameters for the "subset" fits. All the parameters differ systematically from subset to subset, increasing as the normal force increases. Some variation of the fitted values was not unexpected since the pin surface is affected by wear, deteriorating after each run.

In all cases, the values of $a$ and $b$ are rather similar. As mentioned previously, a low value of $(a - b)$ has two effects: a low slope of the

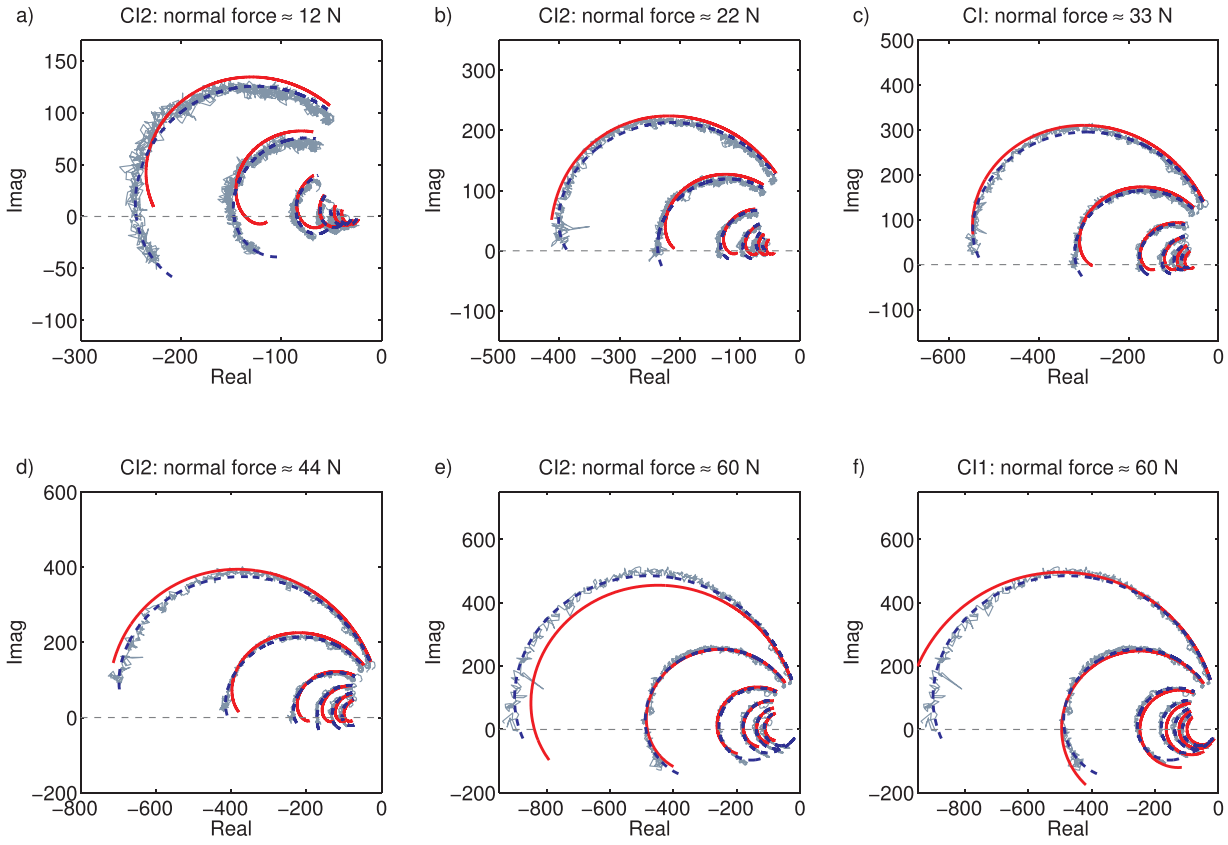


**Fig. 21.** Tufnol on glass: individual fit (blue dashed line) and "subset" fit (red solid line). The $\beta(\omega)$ measurements are referred to different sliding speeds, 1–10 mm/s, and different normal forces; a-e) fitting results obtained using model CI2; f) fitting results obtained using model CI1. (For interpretation of the references to colour in this figure caption, the reader is referred to the web version of this paper).

**Table 3**
Tufnol on glass: identified model parameters obtained by fitting each set of $\beta(\omega)$ measured at a fixed normal force. Model CI1 and CI2 have been used.

| Parameters | Model CI2 | | | | | Model CI1 |
|---|---|---|---|---|---|---|
| | 12 N | 22 N | 33 N | 44 N | 60 N | 60 N |
| $a$ | 0.035 | 0.027 | 0.024 | 0.024 | 0.019 | 0.018 |
| $b$ | 0.017 | 0.009 | 0.008 | 0.008 | 0.013 | 0.017 |
| $t_\phi$ (msec) | 0.2 | 0.3 | 0.5 | 0.5 | 1.5 | – |
| $L$ ($\mu$m) | – | – | – | – | – | 4.8 |

coefficient of sliding friction, and an expansion of the Nyquist plot towards the negative half-plane and eventually towards the right-hand half-plane. Both features are clearly seen in the experimental data. Fig. 23b shows a rather flat slope of the $\mu_{ss}$ curve measured at 1 and 2 mm/s. On the other hand, Fig. 24 exhibits Nyquist plots that straddle the upper and lower half-planes, with a tendency of the lower frequencies to extend towards the right half-plane.

For completeness, it is interesting to check the last two $\beta(\omega)$ measurements performed at 36 N, corresponding to sliding speeds of 2 and 1 mm/s (see Fig. 23b). The value of $\mu_{ss}$ for both curves is around 0.7, almost twice the starting value related to the first measurement of the sequence. However, the corresponding $\beta(\omega)$ curves are fairly similar, as shown in Fig. 25: the solid blue lines are related to the last two measurements, the grey ones to the first two measurements of the equivalent sequence. The level of repeatability is by no means as impressive as has been seen previously, but both pairs of $\beta(\omega)$ are reasonably consistent despite the effects of wear (and perhaps temperature). Fig. 25a also shows the fitting results: as before, each dashed blue line is an individual fit and the solid red line a "subset" fit. Both simulations match the experimental data quite well. The identified model parameters are listed in the last column of Table 4. For this case, $a$ and $b$ are extremely close to each other, with $b$ being slightly higher. This fits the pattern seen in the Nyquist plot in Fig. 25a, where the lowest frequency (100 Hz) reaches the imaginary axis.

### 4.7. Steel on steel: dry and lubricated friction

Steel on steel, either dry or lubricated, is one of the most common material combinations for sliding or rolling contact in mechanical engineering systems. It is thus of interest to test this combination in the dynamic friction rig. While the previous material combinations were regarded mainly as proofs of concept for the technique and its interpretation, this new case goes beyond that by having direct relevance to many applications. A mild steel pin was run against the hardened steel disc, and measurements for different sliding speeds and normal forces were performed. In this case, it is useful to show results over an extended frequency range up to 4 kHz. An example of a lubricated condition was created by spraying a low-viscosity commercial lubricant (WD-40) onto the steel disc. The results of these dry and lubricated friction tests will be illustrated and compared. First, Fig. 26 shows the estimated steady-sliding coefficient of friction: strikingly, $\mu_{ss}$ seems to be quite independent of sliding speed for both cases, while the typical value of the friction coefficient dropped from 0.5 to 0.2 under lubricated conditions.

Before examining the measurements of $\beta(\omega)$ it is useful to summarise the key features of the earlier results. All the dynamic friction measurements for polymer pins against glass or steel showed two significant deviations from a simple Coulomb-type friction law:

a) evidence of internal dynamics was observed, which was taken into account through a state variable and its state-evolution law;
b) $\beta(\omega)$ showed a non-trivial dependence on the normal load, which was tackled by introducing contact stiffness into the model.

The results involving steel on steel add a new piece of information to the story. Fig. 27 shows the $\beta(\omega)$ curves corresponding to the measurements described before. The first thing that may be noticed is that the peaks previously identified as deriving from rig artefacts are now much more prominent. Presumably the combination of the relatively rough steel disc and the relatively hard steel pin results in a higher level of background noise, exciting the rig resonances more strongly. However, although these peaks are distracting to the eye, they should be ignored for the purposes of interpretation, and only the background trends considered. Furthermore, that background "trend" in most cases is approximately a flat horizontal line. In this case, no attempt was made to remove the effects of the rig resonances: it was feared that the required corrections would be large enough that they might distort the underlying data.

The magnitude plots (Figs. 27a– b) demonstrate excellent repeatability of the measurements. The light grey lines, relating to the measurements done by decreasing the sliding speed, are scarcely visible because they match very closely the first sequence of measurements obtained by increasing the sliding speed. Perhaps the most important feature, though, is the fact that the measured $\beta(\omega)$ is virtually independent of frequency. This is true of the complex values, not just the magnitude, as can be seen by inspecting the real (Figs. 27c– d) and imaginary parts (Figs. 27e– f). The real part shows a different but constant amplitude for each sliding speed, while the imaginary part is close to zero. This explains why Nyquist plots are not shown for this case: the points simply cluster in a cloud around each constant value.

Further tests were carried out for different normal forces at a fixed sliding speed (2 mm/s). Figs. 28a–b show the results for $\beta(\omega)$ measured under dry and lubricated conditions, respectively. The constant trend of the amplitude is plain in all cases. The results measured for lubricated friction show smoother curves than the ones measured for dry friction, but apart from that the two groups of curves are remarkably similar. Figs. 28c– d show a scaled version of the measurements (called $\epsilon(\omega)$ in [36,37]), obtained by dividing each $\beta(\omega)$ measurement by the corresponding normal load. In both cases the $\epsilon(\omega)$ plots all collapse to a single curve, demonstrating that the frictional frequency response

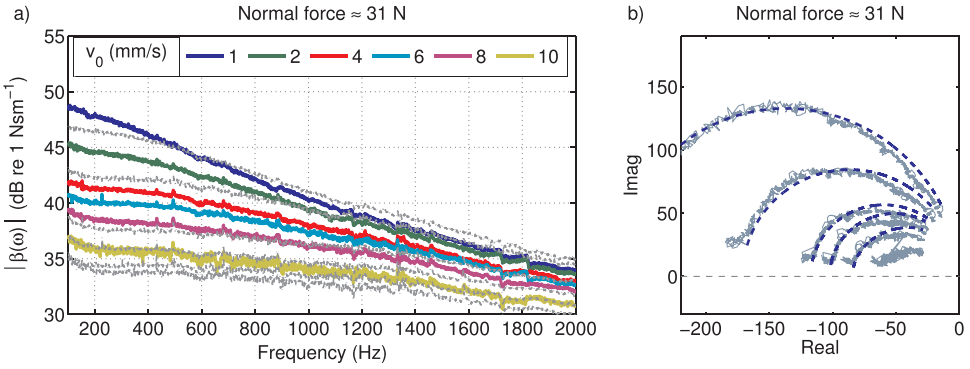


**Fig. 22.** PTFE on glass: a) magnitude plots of $\beta(\omega)$ for different sliding speeds at a fixed normal force of 31 N; b) Nyquist plots of $\beta(\omega)$ and fitting results obtained using model CI1. (For interpretation of the references to colour in this figure caption, the reader is referred to the web version of this paper).

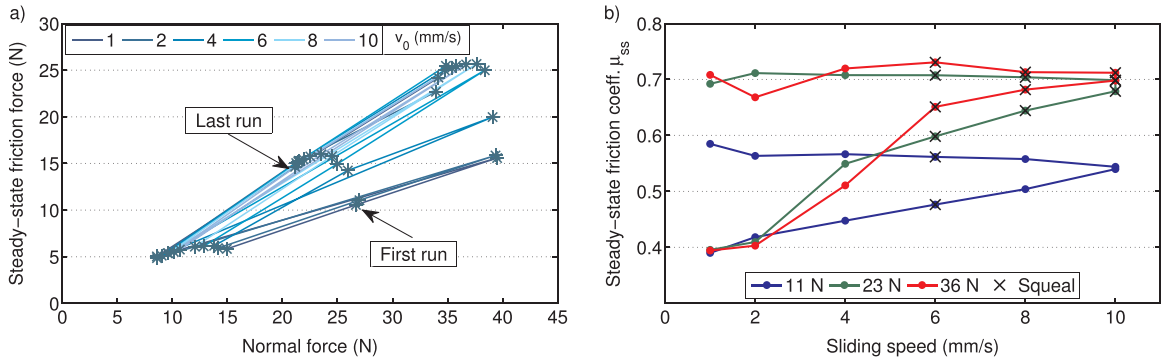


**Fig. 23.** Polycarbonate on steel: a) friction force against normal force for different sliding speeds. For the sequence at 23 N, the first and last runs are indicated by arrows to highlight the normal force variation during the sequence of tests; b) measurements of $\mu_{ss}$ for different sliding speeds and normal forces. The cross symbols refer to measurements where squeal occurred. (For interpretation of the references to colour in this figure caption, the reader is referred to the web version of this paper).

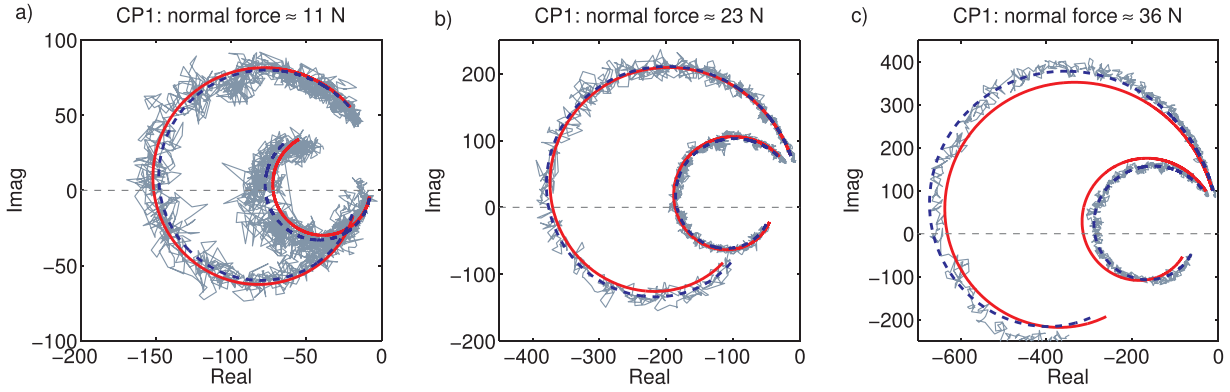


**Fig. 24.** Polycarbonate on steel: a-c) individual fit (blue dashed line) and "subset" fit (red solid line). The $\beta(\omega)$ measurements are referred to two sliding speeds, 1 and 2 mm/s, different normal forces, and to a frequency range between 100–2000 Hz. Fitting results obtained using model CP1. (For interpretation of the references to colour in this figure caption, the reader is referred to the web version of this paper).

**Table 4**
Polycarbonate on steel: identified model parameters obtained by fitting each "subset" of $\beta(\omega)$ measured at a fixed normal force. Model CP1 has been used.

| Parameters | $\beta(\omega)$ 1–2 mm/s | | | $\beta(\omega)$ 2–1 mm/s |
|---|---|---|---|---|
| | 11 N | 23 N | 36 N | 36 N |
| $a$ | 0.012 | 0.017 | 0.019 | 0.021 |
| $b$ | 0.010 | 0.014 | 0.015 | 0.022 |
| $L$ ($\mu$m) | 0.177 | 0.396 | 0.606 | 0.322 |
| $k_t$ (MN/m) | 0.696 | 0.982 | 1.270 | 1.370 |

functions for these steel on steel tests exhibit a simple proportional relationship with the normal load (as suggested by the Amontons-Coulomb law).

At first glance, the conclusion would be that the dynamic frictional

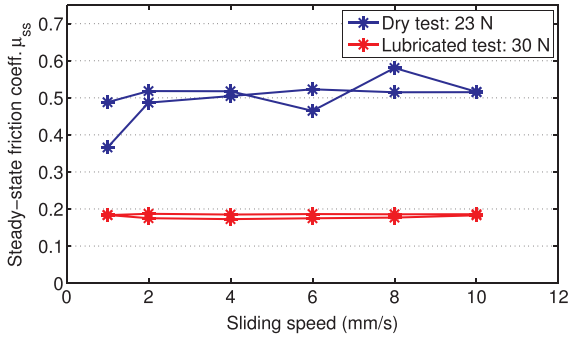


**Fig. 26.** Steel on steel: dry friction (blue line) and lubricated friction (red line) measurements of $\mu_{ss}$ for different sliding speeds and a fixed normal force, 23 N and 30 N respectively. (For interpretation of the references to colour in this figure caption, the reader is referred to the web version of this paper).

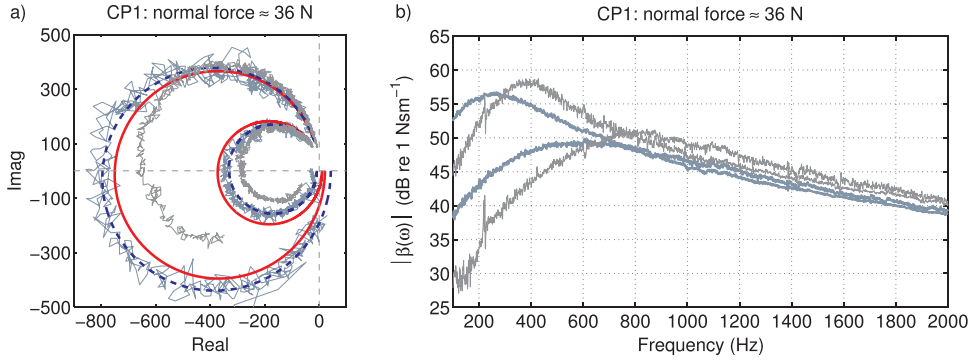


**Fig. 25.** Polycarbonate on steel: The blue solid curves refer to the last two $\beta(\omega)$ of the sequence measured at 36 N, the grey curves to the first two $\beta(\omega)$ of the same sequence (Fig. 24c). For each pair of measurements, the one with the higher amplitude has been measured at 1 mm/s, the other at 2 mm/s. a) Nyquist plot and fitting results obtained using model CP1 (individual fit: blue dashed line, "subset" fit: red solid line); b) magnitude plot. (For interpretation of the references to colour in this figure caption, the reader is referred to the web version of this paper).

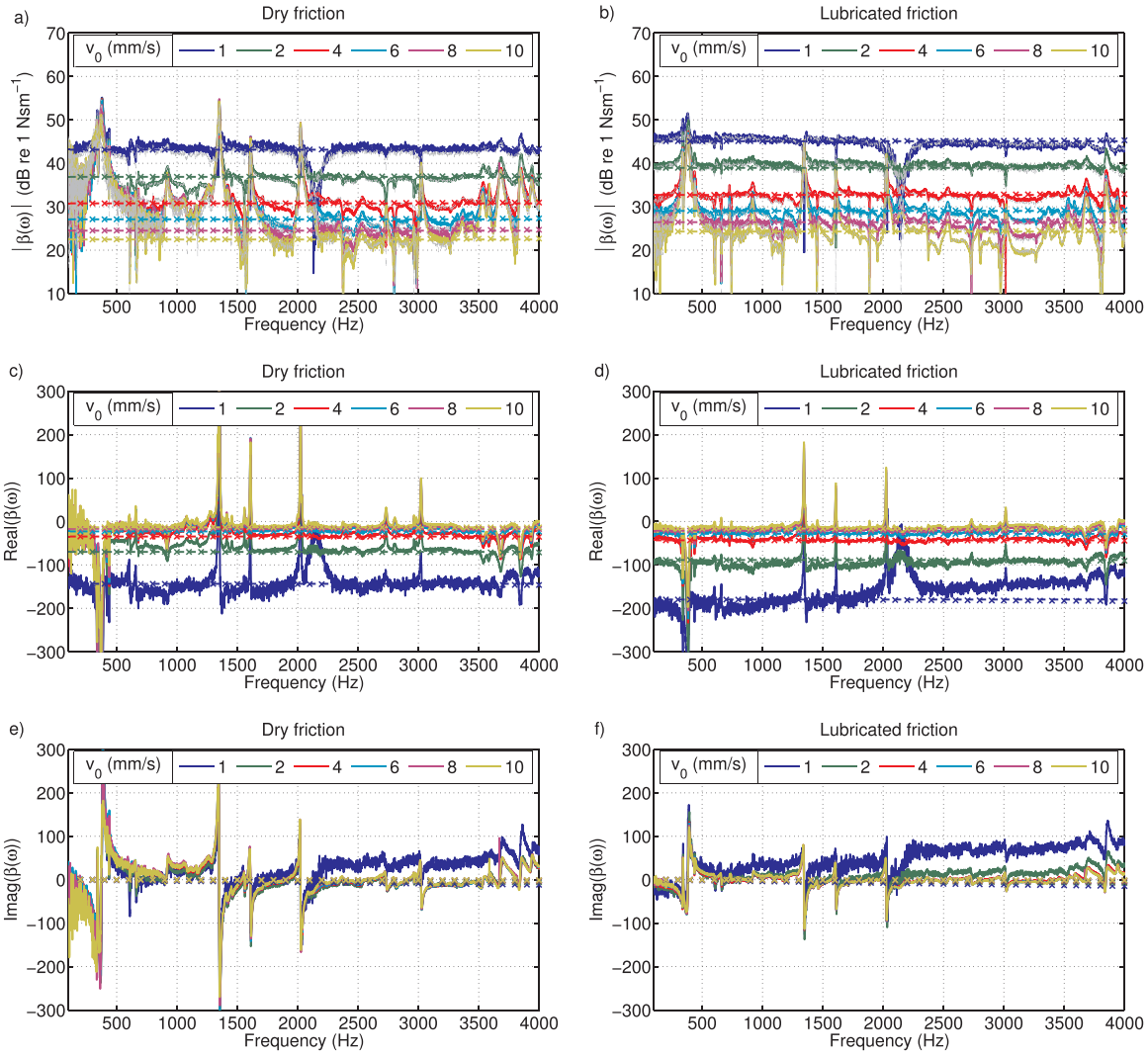


**Fig. 27.** Steel on steel: frictional frequency response function measured for different sliding speeds (1–10 mm/s) and with a fixed normal force at 23 N for dry friction tests (a, c and e), and at 30 N for lubricated friction tests (b, d and f); (a)–(b) magnitude plot; (c)–(d) real part plot;(e)–(f) imaginary part plot. The coloured horizontal dashed lines indicate the predicted $\beta(\omega)$ by using a rate-dependent friction model (11), with value $a = 0.0058$. The corresponding crosses indicate the predicted $\beta(\omega)$ by using a rate-and-state friction model (12), with value $a = 0.0078$, $b = 0.002$ and $t_\phi = 0.01$ms. (For interpretation of the references to colour in this figure caption, the reader is referred to the web version of this paper).

behaviour of steel sliding on steel seems to depend only on sliding speed. In a first attempt to test this against modelling, the state variable of the rate-and-state model from Eq. (4) can be "frozen" and only the rate-dependent term retained. The contact stiffness was also neglected (by regarding it as infinite). The frictional frequency response function then reads:

$$\beta(\omega) = -\frac{aN_0}{v_0} \tag{11}$$

which corresponds to the slope of Eq. (8) if the state variable is neglected. This simple formula is consistent with all the measurements. A suitable value of $a$ has been obtained in each case by simple manual tuning. Dashed horizontal lines in Figs. 27a– d show the predictions of Eq. (11) with the value $a = 0.0058$: the level of $\beta(\omega)$ is quite well matched for each different sliding speed and normal force. It is striking that both the dry and lubricated friction tests can be predicted remarkably well using the same value of this parameter. Recall that the measured values of $\mu_{ss}$ were very different under the two conditions, although the very low slope of curves was quite similar. The dashed lines in Figs. 28a– b were obtained by using model parameter $a = 0.009$ for the dry friction tests, and $a = 0.007$ for the lubricated tests: slightly different values seem to work best in this case, but it would require more extensive data to determine whether this is a real difference or simply a manifestation of uncertainty in the fitting process.

It is also possible to analyse these results in terms of the rate-and-state models discussed earlier. Rather than "freezing" the state variable as in Eq. (11), it can be retained but assigned a time constant that is very short compared to the ones obtained for the polymer cases (see Fig. 14b). In any case, it seems to be admissible to neglect the elastic contribution. Therefore, a second modelling attempt consisted in simulating the observed data by using only the rate-and-state version of $\beta(\omega)$ given by:

$$\beta_{RS}(\omega) = -\frac{g_{,\phi} f'_{ss} + i\omega f_{,v}}{g_{,\phi} + i\omega} \text{ (RSmodel)} \tag{12}$$

According to Table 1, the fitting parameters here are $a$, $b$ and $t_\phi$. The predictions for dry and lubricated friction are shown by the cross markers plotted in Figs. 27a– f. The values of $a$ and $b$, 0.0078 and 0.002 respectively, have been chosen such that the difference $(a - b)$ would correspond to the identified value of $a$ if only the rate model (11) is used. The time-scale variable $t_\phi$ is equal to 0.01 ms, around two order of magnitudes lower than the ones identified in Fig. 14b. It was found that any value lower than 0.01 ms would provide similar results, closely matching those of the rate-only model (11). Similarly, the coloured

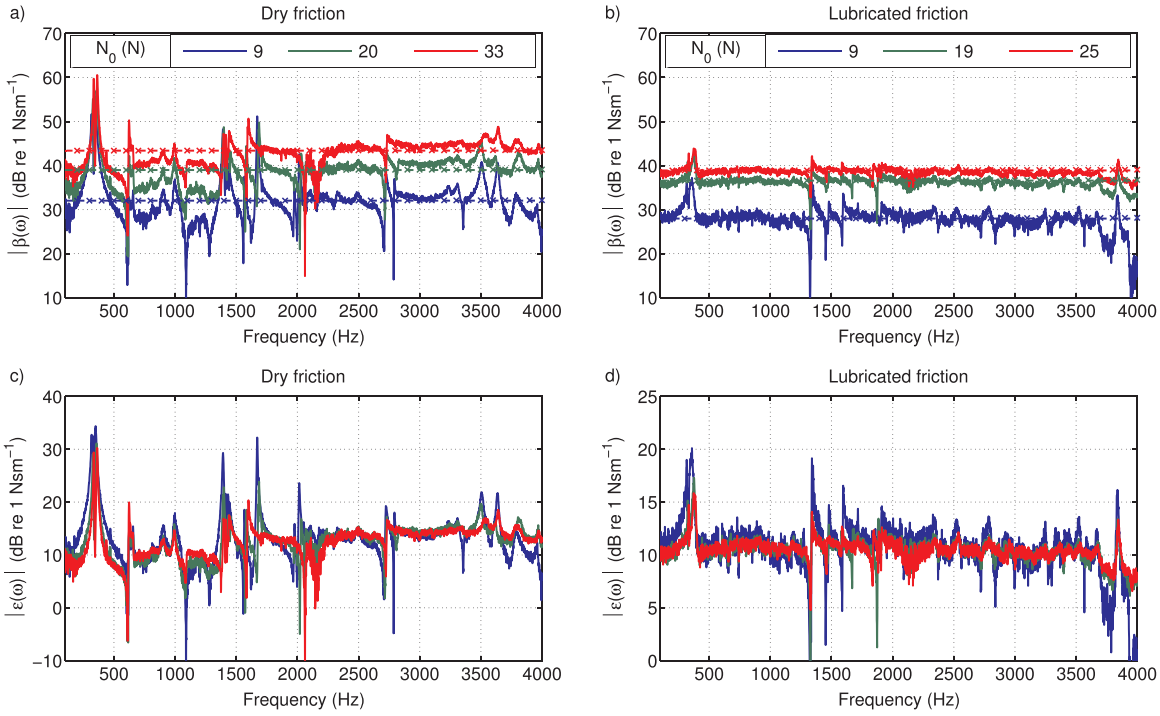


**Fig. 28.** Steel on steel: frictional frequency response function with a fixed sliding speed of 2 mm/s, measured at different normal forces (9, 20 and 33 N) for dry friction tests (a and c), and (9, 19 and 25 N) for lubricated friction tests (b and d); (a)–(b) $\beta(\omega)$ measurements; (c)–(d) $\varepsilon(\omega)$ measurements. The coloured horizontal dashed lines indicate the predicted $\beta(\omega)$ by using a rate-dependent friction model (11), with values $a = 0.009$ and $a = 0.007$, for dry and lubricated tests respectively. The corresponding crosses indicate the predicted $\beta(\omega)$ by using a rate-and-state friction model (12), with value $a = 0.011$ and $a = 0.009$ for dry and lubricated tests respectively. The time-scale $t_\phi$ and the value of $b$ shown in Fig. 27 were adopted. (For interpretation of the references to colour in this figure caption, the reader is referred to the web version of this paper).

cross markers in Figs. 28a–b were obtained by using $a = 0.011$ and $a = 0.009$ for dry and lubricated friction, respectively. The same values of $b$ and $t_\phi$ used in Fig. 27 were adopted.

In terms of the results shown here, the implication is that the simpler model (11) seems preferable to the more complicated one (12). The reason that both have been included in this discussion is that it may well turn out, if alternative dynamic friction tests are carried out with the same contacting materials, that evidence of the state variable decay rate might emerge. For example, many tests relating to rock mechanics and earthquake modelling use sudden jumps in sliding speed to give direct visualisation of the exponential transient associated with a state variable (see for example [14]).

A final remark can be made about $\beta(\omega)$ measured at 1 mm/s for both dry and lubricated tests, as shown in Fig. 27. The imaginary part in this case shows a slight positive slope, and according to Eqs. (5) and (6) this effect could be predicted by re-introducing the contact stiffness. However, the measured results are not sufficiently clear to demonstrate the need for contact stiffness unambiguously.

## 5. Discussion and conclusions

In a previous paper ([1]), it was suggested that measurements of the frictional frequency response $\beta(\omega)$ could be explained by a version of the rate-and-state friction law, incorporating some allowance for contact stiffness. However, that conclusion was based on very limited data. In the present work a much wider range of material combinations has been tested, and it has been demonstrated that some version of the proposed family of closely-related models can fit well in every case.

Furthermore, the methodology for measurement, model discrimination and parameter identification has been significantly enhanced. Additional measurement methods have been introduced that provide cross-checks and improved robustness. One major target was to strengthen model discrimination. It has been argued previously ([36,37,1]) that $\beta(\omega)$ gives a kind of "fingerprint" of the sliding interface between the tested materials. It provides the required input for a complex eigenvalue analysis of the stability of systems (like vehicle brakes) containing a sliding interface, but in addition it gives an efficient and powerful tool to discriminate among candidate constitutive models for dynamic friction. In the present work it has been shown that the measured frictional frequency response can be used to discriminate successfully between variants of the enhanced rate-and-state model that differ only in relatively subtle ways.

Results have been shown for a variety of polymer-based pins (nylon, polycarbonate, PMMA, PTFE and Tufnol) sliding against a glass disc, and also for polycarbonate and steel pins sliding against a steel disc. For the steel-on-steel case, tests were made both dry and lubricated. The frictional frequency response function has been measured systematically over a range of normal forces (10–60 N), of sliding speeds (1–10 mm/s) and for frequencies up to at least 2 kHz. In parallel, the steady-sliding friction force was also measured under the same range of conditions. The large set of material combinations now explored gives insight into the range of variation of the measured $\beta(\omega)$, and of the parameters of models fitted to those measurements. The measured $\beta(\omega)$ seems in general to be far more robust than the estimated coefficient of sliding friction, and for some material sets it is very strikingly repeatable.

Some material sets exhibited a high wear rate (particularly PTFE on glass and polycarbonate on steel), but even those showed reasonably consistent behaviour of $\beta(\omega)$. For the future, it may be useful to try measurements using cylindrical pin samples, with a flat contact surface, rather than the hemispherical pins used here. This might improve the repeatability of $\beta(\omega)$, since the nominal area of contact would remain approximately constant even in the presence of wear. In any case, from a pragmatic point of view it would be useful to know whether satisfactory measurements of $\beta(\omega)$ can be obtained using such flat-faced pin samples since these are the kind normally used in commercial tribological test machines. Tests of this kind might then become more easily available to, for example, the automotive industry and

geomechanical community.

For all the tests using polymeric pins, a model incorporating both an internal state variable and a contact stiffness was necessary. In cases where wear was not an issue, it was possible to find a single model capable of fitting subsets of the measurement matrix, or even the entire matrix covering different sliding speeds and normal loads. In other words, the selected models captured the parameter dependence as well as the frequency dependence of $\beta(\omega)$. Furthermore, the parameter values of the fitted models showed a good degree of consistency between materials: see for example Figs. 14 and 15.

The results for steel on steel, however, provided a surprise. In this case the results first suggested that the friction force depends only on the instantaneous sliding speed: virtually no frequency dependence was seen, and also the $\beta(\omega)$ curves scaled directly with the normal load, as the familiar but naive Coulomb law would suggest. The value of $\beta(\omega)$ for given values of $v_0$ and $N_0$ should then be simply the slope of the steady-sliding force-velocity curve at the operating point $v_0$: a real number, independent of frequency. However, it has been shown that similar behaviour can be obtained with a rate-and-state model provided the time-scale parameter $t_\phi$ has a sufficiently low value. The introduction of the state variable makes $\beta(\omega)$ complex, even though the amplitude and phase exhibit only very small variation with frequency over the range explored here. The smaller time-scale suggests that the "rejuvenation" time of the contact asperities for the metal on metal case is at least two order of magnitudes faster than for the polymer cases.

Parameter identification for a model depending only on slip-rate is very straightforward. Simple manual tuning gave satisfactory estimates of parameter $a$ for the steel-on-steel material combination, and this was the only variable required. On the other hand, frequency-dependent $\beta(\omega)$ requires cross-validations in order to provide a robust identification of the different fitting parameters. For the latter case, the parameters inferred from alternative tests — steady-sliding tests and "direct" contact stiffness measurements without rotation of the disc — have been used, either to corroborate or to integrate with the parameter estimation process based on the $\beta(\omega)$ measurement. For example, the identified parameters $a$ and $b$, obtained by comparing the rate-and-state model with the $\beta(\omega)$ measurements, have been shown to be consistent with values inferred from the slope of the corresponding steady-sliding force–velocity curve. In a similar way, the contact stiffness for the polymer samples turned out to be quite consistent between the two different kinds of test, both in magnitude and power law dependence on the normal load.

In terms of modelling, a major target was to probe the limits of applicability of the family of related friction laws proposed in [1]. Only a subset of the earlier set of models has been explored here: the monotonic models, but not the non-monotonic ones. This choice was mainly determined by the available range of data: a proper validation of a non-monotonic model would require measurements over a larger range of sliding speeds, and this is a topic of ongoing research. It has been shown that each measured $\beta(\omega)$ function, considered individually, can be accurately reproduced by the proposed rate-and-state model. However, to reach a clear conclusion about whether a fixed length-scale or a fixed time-scale gave a better description to represent the state-variable dynamics, a different fitting strategy was required: "subset" or "data-matrix" fits allow discrimination between the two cases.

This strategy worked well except for the case of PTFE on glass, which pushed the proposed validation methodology to its limit. Three factors may have caused this issue: 1) the high level of noise in the data; 2) the pronounced wear effect; 3) the limitation of the optimisation method used. In the current paper, constrained and unconstrained gradient-based optimisation methods have been used. Possibly, more complex optimisation methods such as genetic algorithms or neural networks could have provided more robust results for the PTFE case, but testing the performance of different optimisation algorithms in order to highlight subtle differences between the different versions of the rate-and-state models has not been the aim of the current paper. The main focus has addressed, in demonstrating the discriminatory value of the $\beta(\omega)$ measurement.

In the light of the results shown here, promising directions for future work can be mapped out quite easily. It would be valuable to extend the experimental methodology further by including additional tests which can be made in the same apparatus and under the same contact conditions: examples of types of test used in other contexts are forced reciprocating sliding, sudden jumps between different steady sliding speeds, and steady sliding over a larger velocity range. An enhanced repertoire of testing of this kind would provide additional information, especially for the identification of the state variable, and allow the proposed family of models to be tested more thoroughly (e.g. the non-monotonic rate-and-state models). A natural next step would be to explore whether the fitted model is capable of accurate prediction of instability thresholds, such as the pattern of squeal occurrences shown in Fig. 23b.

So far, the friction testing has only involved the tangential direction, parallel to the sliding velocity at the contact point. However, [30] have suggested that a more general approach to the stability of systems with a sliding point contact should also include similar frequency-response information relating to normal force and velocity fluctuations. This would lead to a general linearised contact model involving a $2 \times 2$ matrix of which $\beta(\omega)$ is one entry. It might be of great interest to extend the measurement procedure to identify experimentally each term of this $2 \times 2$ matrix, to assess the outcome in terms of physical models, and to explore the influence on the prediction of dynamic friction-driven vibration.

Finally, it is worth suggesting that the experimental methodology set out here could be transferred to industrial applications. Many industries make use of tribological test equipment to quantify the behaviour of interfaces, and it should be possible to extend those tests to investigate the dynamic quantities discussed here. That in turn might lead to more reliable predictions of such phenomena as brake squeal.

## Acknowledgements

The authors thank Thibaut Putelat for many helpful discussions, Alex Casabuena Rodriguez for assistance with the scanning electron microscopy for Fig. 13, and Neil Houghton for his crucial contribution to design and construction of the test rig. Financial support was provided by the EPSRC programme grant "Engineering Nonlinearity" (ref. EP/K003836/1 — www.engineeringnonlinearity.ac.uk). All data associated with this paper can be found in the University of Cambridge Repository: https://dx.doi.org/10.17863/CAM.12973

## Appendix A. Linearity checks

In order to justify the linear assumption upon which the $\beta(\omega)$ measurement relies, the perturbed velocity should always be lower than the nominal sliding speed $v_0$ of the pin on the disc. Evidence for linearity has been discussed elsewhere ([36]), but for completeness some results are shown here. The levels of excitation provided by the piezo actuator can be adjusted by changing the drive voltage. Several different levels have been tested, and three of them are illustrated in Fig. 29a for the case of a nylon pin on a glass disc. The cases are labelled V3, V4 and V5, where V5 is the highest level the rig hardware can safely deliver. The sliding speed of the disc was fixed at 2 mm/s for these particular tests. Fig. 29b shows the Nyquist plots obtained for the different voltages. Excellent agreement among all three curves was obtained: the $\beta(\omega)$ curves are identical in both amplitude and phase to within the noise limits of the measurement. This demonstrates that linearisation seems to be remarkably robust, even when

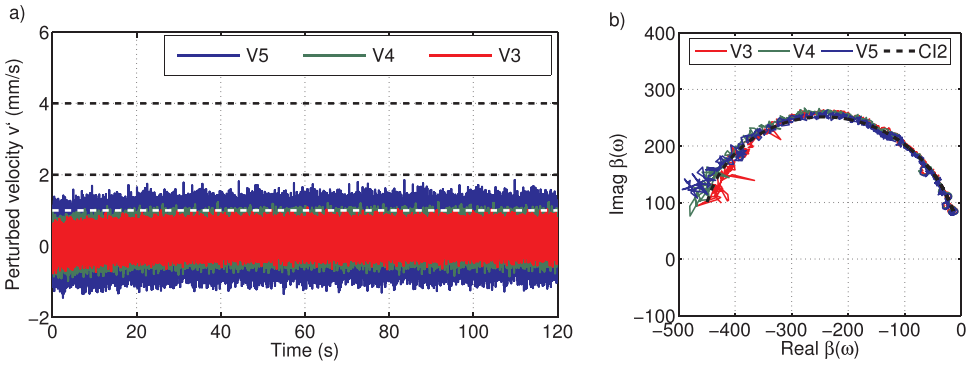


**Fig. 29.** Nylon on glass: measurements of $\beta(\omega)$ at different input amplitudes. (a) Time series of the perturbed velocity $v'$. The three dashed lines indicate the lowest nominal sliding speeds of the disc used in these tests: 1, 2 and 4 mm/s. (b) Corresponding Nyquist plots measured at 2 mm/s. The dashed black line represents the fit obtained by model CI2.

the perturbation velocity occasionally comes close to the disc velocity.

The measurements reported in this paper were all performed at the highest drive voltage, V5, for sliding speeds $\geq$ 2 mm/s. However, for the cases of $\beta(\omega)$ measured at a sliding speed of 1 mm/s, the drive voltage was reduced to the level V3. This choice of the highest reasonable voltage setting in every case was made in order to maximise the signal-to-noise ratio in the results.

## References


[1] A. Cabboi, T. Putelat, J. Woodhouse, The frequency response of dynamic friction: enhanced rate-and-state models, J. Mech. Phys. Solids 92 (2016) 210–236.
[2] R.A. Ibrahim, Friction-induced vibration, chatter, squeal, and chaos. Part II: dynamics and modeling, Appl. Mech. Rev. 47 (7) (1994) 227–253.
[3] M. Graf, G.-P. Ostermeyer, Friction-induced vibration and dynamic friction laws: Instability at positive friction-velocity-characteristic, Tribol. Int. 9 (2015) 255–258.
[4] P.J. Blau, Friction Science and Technology: from Concepts to Applications, CRC Press, Taylor and Francis, Boca Raton, USA, 2009.
[5] J.A. Greenwood, J.B.P. Williamson, Contact of nominally flat surfaces, Proc. R. Soc. Lond. A: Math., Phys. Eng. Sci. 295 (1442) (1966) 300–319.
[6] H. Dankowicz, On the modeling of dynamic friction phenomena, ZAMM Z. fur Angew. Math. Mech. 79 (6) (1999) 399–409.
[7] A.P. Merkle, L.D. Marks, A predictive analytical friction model from basic theories of interfaces, contacts and dislocations, Tribol. Lett. 26 (1) (2007) 73–84.
[8] M. Ciavarella, J. Greenwood, M. Paggi, Inclusion of interaction in the Greenwood and Williamson contact theory, Wear 265 (56) (2008) 729–734.
[9] K. De Moerlooze, F. Al-Bender, H.Van Brussel, A generalised asperity-based friction model, Tribol. Lett. 40 (1) (2010) 113–130.
[10] M. Eriten, A.A. Polycarpou, L.A. Bergman, A physics-based friction model and integration to a simple dynamical system, J. Vib. Acoust. 134 (5) (2012) 051012/1–051012/9.
[11] V.L. Popov, L. Voll, Q. Li, Y.S. Chai, M. Popov, Generalized law of friction between elastomers and differently shaped rough bodies, Sci. Rep. 4 (2014) 3750.
[12] B. Jacobson, The Stribeck memorial lecture, Tribol. Int. 36 (11) (2003) 781–789.
[13] G. Sheng, Friction-induced Vibrations and Sound: Principles and Applications, CRC Press, Taylor and Francis, Boca Raton, USA, 2008.
[14] J.H. Dieterich, Modeling rock friction: 1. experimental results and constitutive equations, J. Geophys. Res. 84 (1979) 2161–2168.
[15] A.L. Ruina, Slip instability and state variable friction laws, J. Geophys. Res. 88 (1983) 10359–10370.
[16] T. Putelat, J.H.P. Dawes, J.R. Willis, On the microphysical foundations of rate-and-state friction, J. Mech. Phys. Solids 59 (5) (2011) 1062–1075.
[17] Y. Bar-Sinai, R. Spatschek, E.A. Brener, E. Bouchbinder, Velocity-strengthening friction significantly affects interfacial dynamics, strength and dissipation, Sci. Rep. 5 (2015) 7841.
[18] T. Putelat, J.H.P. Dawes, Steady and transient sliding under rate-and-state friction, J. Mech. Phys. Solids 78 (2015) 70–93.
[19] C. Canudas deWit, H. Olsson, K. Astrom, P. Lischinsky, A new model for control of systems with friction, IEEE Trans. Autom. Control 40 (3) (1995) 419–425.
[20] A. Saha, P. Wahi, M. Wiercigroch, A. Stefaski, A modified LuGre friction model for an accurate prediction of friction force in the pure sliding regime, Int. J. Non-Linear Mech. 80 (2016) 122–131.
[21] F. Al-Bender, V. Lampaert, J. Swevers, The generalized maxwell-slip model: a novel model for friction simulation and compensation, IEEE Trans. Autom. Control 50 (11) (2005) 1883–1887.
[22] K. Jankowski, A. Saha, A. Stefański, Introduction of novel model of friction and analysis of presliding domain of friction with non-local memory effect based upon Maxwell slip model structures, Tribol. Int. 102 (2016) 378–391.
[23] J. Woodhouse, T. Putelat, A. McKay, Are there reliable models of friction? Philos. Trans. R. Soc. A: Math. Phys. Eng. Sci. 373 (2015).
[24] C.H. Scholz, Earthquakes and friction laws, Nature 391 (1998) 37–41.
[25] H. Kawamura, T. Hatano, N. Kato, S. Biswas, B.K. Chakrabarti, Statistical physics of fracture, friction, and earthquakes, Rev. Mod. Phys. 84 (2012) 839–884.
[26] A. Bizzarri, The mechanics of seismic faulting: recent advances and open issues, Riv. Del Nuovo Cim. 37 (2014) 181–271.
[27] J. Woodhouse, P. Galluzzo, The bowed string as we know it today, Acta Acust. United Acust. 90 (4) (2004) 579–589.
[28] P. Galluzzo, J. Woodhouse, H. Mansour, Bowed-string transients: comparison of measurement and simulations, Acta Acustica united with Acustica (Submitted for publication).
[29] H. Hetzler, K. Willner, On the influence of contact tribology on brake squeal, Tribol. Int. 46 (1) (2012) 237–246.
[30] T. Butlin, J. Woodhouse, Friction-induced vibration: model development and comparison with large-scale experimental tests, J. Sound Vib. 332 (21) (2013) 5302–5321.
[31] C.W. Schwingshackl, E.P. Petrov, D.J. Ewins, Effects of contact interface parameters on vibration of turbine bladed disks with underplatform dampers, J. Eng. Gas Turbines Power 134 (3) (2012) 032507.
[32] C. Gastaldi, M.M. Gola, On the relevance of a microslip contact model for underplatform dampers, Int. J. Mech. Sci. 115–116 (2016) 145–156.
[33] N. Kinkaid, O. O'Reilly, P. Papadopoulos, Automotive disc brake squeal, J. Sound Vib. 267 (1) (2003) 105–166.
[34] N.P. Hoffmann, L. Gaul, Friction induced vibrations of brakes: Research fields and activities, in: SAE Technical Paper, SAE International, 2008, paper No. 2008-01-2579, Warrendale, PA.
[35] C. Cantoni, R. Cesarini, G. Mastinu, G. Rocca, R. Sicigliano, Brake comfort a review, Veh. Syst. Dyn. 47 (8) (2009) 901–947.
[36] S. Wang, J. Woodhouse, The frequency response of dynamic friction: a new view of sliding interfaces, J. Mech. Phys. Solids 59 (5) (2011) 1020–1036.
[37] J. Woodhouse, S. Wang, The frequency response of dynamic friction: model comparisons, J. Mech. Phys. Solids 59 (11) (2011) 2294–2306.
[38] K.G. McConnel, P.S. Varoto, Vibration Testing: Theory and Practice, 2nd Ed., Wiley, Hoboken, USA, 2008.
[39] K.L. Johnson, Contact Mechanics, Cambridge University Press, Cambridge, UK, 1985.
[40] M. Gonzalez-Valadez, A. Baltazar, R. Dwyer-Joyce, Study of interfacial stiffness ratio of a rough surface in contact using a spring model, Wear 268 (34) (2010) 373–379.
[41] S. Medina, D. Nowell, D. Dini, Analytical and numerical models for tangential stiffness of rough elastic contacts, Tribol. Lett. 49 (1) (2013) 103–115.
[42] C. Cattaneo, Sul Contato di due Corpo Elastici, 27(6) Rendiconti dell'Accademia naionale dei Lincei, 1938 (342348,434436, 474478).
[43] R.D. Mindlin, Compliance of elastic bodies in contact, Trans. ASME Ser. E J. Appl. Mech. 16 (259) (1949) 259–268.
[44] I. Etsion, Revisiting the Cattaneo-Mindlin concept of interfacial slip in tangentially loaded compliant bodies, J. Tribol. 132 (2) (2010) (020801–1–020801–9).
[45] W.W.S. Wei, Time Series Analysis: Univariate And Multivariate Methods, 2nd Ed., Addison Wesley, Boston, USA, 2006.